C h a p t e r 2

Manganese-oxidizing photosynthesis before the rise of cyanobacteria

Jena E. Johnson[a], Samuel M. Webb[b], Katherine Thomas[c], Shuhei Ono[c], Joseph L. Kirschvink[a], Woodward W. Fischer[a]

[a]Division of Geological and Planetary Sciences, California Institute of Technology, Pasadena, CA 91125. [b]Stanford Synchrotron Radiation Lightsource, Menlo Park, CA 94025. [c]Department of Earth, Atmospheric and Planetary Sciences, Massachusetts Institute of Technology, Cambridge, MA 02139.

Originally published in the Proceedings of the National Academy of Sciences, Volume 108, p. 11238-11243

ABSTRACT

The emergence of oxygen-producing (oxygenic) photosynthesis fundamentally transformed our planet; however, the processes that led to the evolution of biological water splitting have remained largely unknown. To illuminate this history, we examined the behavior of the ancient Mn cycle using newly-obtained scientific drill cores through an early Paleoproterozoic succession (2.415 Ga) preserved in South Africa. These strata contain substantial Mn-enrichments (up to ~17 wt. %) well before those associated with the rise of oxygen like the ~2.2 Ga Kalahari Mn deposit. Utilizing new microscale X-ray spectroscopic techniques coupled to optical and electron microscopy and carbon isotope ratios, we demonstrate that the Mn is hosted exclusively in carbonate mineral phases derived

from reduction of Mn-oxides during diagenesis of primary sediments. Additional observations of independent proxies for O_2—multiple S isotopes (measured by IRMS and SIMS) and redox-sensitive detrital grains—reveals that the original Mn-oxide phases were not produced by reactions with O_2, pointing to a different high potential oxidant. These results show that the oxidative branch of the Mn cycle predates the rise of oxygen, and provide strong support for the hypothesis that the water-oxidizing complex of photosystem II evolved from a former transitional photosystem capable of single electron oxidation reactions of Mn.

INTRODUCTION

The rise of atmospheric oxygen ~2.4 billion years ago (1, 2) is the most marked environmental change in Earth history, and this transition ultimately stems from a major biological innovation—the evolution of oxygenic photosynthesis (3, 4). Several biochemical attributes were invented to facilitate this metabolism, including a core photosystem pigment with a higher redox potential than other photosynthetic reaction centers (to enable the oxidation of water) and coupled photosystems. The critical photochemical invention, however, was the water oxidizing complex (WOC) of photosystem II (PSII)—a cubane cluster of four redox-active Mn atoms and a Ca atom, bound by oxo bridges (5, 6)—which acts as a capacitor to store oxidizing equivalents and link the single electron photochemistry of the reaction center to the four electron oxidation of two water molecules to molecular oxygen (7).

Several hypotheses for the origin and evolution of the remarkable water-oxidizing machinery have been proposed. Early ideas suggested that a Mn-bearing protein was evolutionarily co-opted to become the WOC. In 1970, Olson recognized the need for transitional electron donors with intermediate redox potentials, proposing a series of nitrogen-bearing compounds such as NO and NO_2^- (8). He hypothesized that a Mn(III)-porphyrin cytochrome replaced a Fe-bearing cytochrome as the first step to evolving a Mn-based WOC (8). This idea has become less plausible as the availability of these transitional N compounds is questionable in a pre-oxygenated world (9), and as our current understanding is that Mn is not bound in a cytochrome but rather a Mn_4CaO_5 cluster (6). Looking to other Mn-bearing proteins as transitional WOCs, Blankenship and Hartman postulated that a Mn-containing catalase transferring electrons from an H_2O_2 donor might have been an intermediate step in the evolution of oxygenic photosynthesis (10). However, there are no significant sequence or structural similarities between the core protein of PSII and Mn catalase, and no evidence for a significant amount of hydrogen peroxide in Archean oceans (10, 11).

A different class of hypotheses suggested that the WOC was derived from the integration of external manganese oxide phases, building on short-range structural similarities between the WOC and certain tunnel-structured Mn-oxide phases like hollandite (11, 12). This hypothesis, however, is at odds with the general dearth of environmental Mn-oxide phases prior to the rise of oxygen (13, 14). Furthermore, this process is not recapitulated during formation of the WOC today, which only requires soluble Mn(II) and light (15).

During modern assembly of the WOC, no O_2 is evolved, but rather electrons are donated from divalent Mn to the photosystem to arrive at the basal oxidation state (S_0) of the water-oxidizing $Mn(III)_3Mn(IV)$ cluster (4, 7). This mechanism of photoassembly offers a potential clue to the evolution of the WOC.

A transitional Mn-oxidizing photosystem prior to oxygenic photosynthesis. From an evolutionary perspective, it is notable that modern biological water-splitting begins with Mn oxidation, and this observation forms the basis for a final class of evolutionary scenarios wherein Mn(II) played an important role as an electron donor for photosynthesis prior to oxygenic photosynthesis. Zubay proposed that anoxygenic Fe-based phototrophs developed the capacity for Mn oxidation, which subsequently evolved into a tetramanganese WOC able to store oxidizing equivalents and perform water oxidation (16). Dismukes and coworkers later hypothesized that $Mn(II)(HCO_3)_x$ complexes offered lower potential donors to a transitional photosystem, which then evolved to contain a tetramanganese cluster via a 'bicarbonate oxidase' intermediate that produced O_2 prior to water splitting (17). Allen and Martin (2007) envisioned a protocyanobacterium which started to receive electrons from soluble Mn(II) oxidized by UV radiation (18). These hypotheses differ in their evolutionary mechanics, but all broadly invoke photooxidation of Mn(II)-bearing compounds prior to the evolution of photochemical water splitting. The high concentrations of Mn(II) in Archean surface seawater (19, 20) would have presented an evolutionary opportunity and electron source for direct Mn(II) oxidation by an early photosystem able to perform one-electron

photochemical reactions. In order to exploit this resource, a primitive reaction center would have needed to produce a higher potential oxidant to strip electrons from Mn—higher than required for other electron donors but closer to that required for water oxidation. Considering these redox potential constraints, Mn oxidation is an attractive photosynthetic donor on a trajectory to oxidizing water (16–18). An initial manganese-oxidizing photosystem also explains both why the only known biological system that can oxidize water originally procures electrons from Mn and why WOC assembly begins with Mn oxidation. This hypothesis makes a clear prediction: were Mn-based photosynthesis ever realized as a transitional state, it should predate the evolution of oxygenic cyanobacteria. This would leave a distinctive mark in the geological record, with the byproduct of photosynthesis (Mn oxides) forming before the rise of cyanobacteria and in the absence of molecular oxygen.

The timing of cyanobacterial origins remains controversial because of the absence of a robust Archean fossil record. The use of molecular fossils was explored with much apparent potential (21). 2.7 Ga biomarkers associated with cyanobacteria, 2-methyl hopanoids, suggested the early rise of cyanobacteria, but the syngeneity of these compounds (22) and their connection to cyanobacteria (23, 24) has since been questioned. A separate, widely applied approach to date the evolution of cyanobacteria centers on proxies for their metabolic product: O_2. A variety of geochemical tracers, such as Mo, Re, steranes, and iron speciation, have been used to argue for very low (~ nanomolar) levels of dissolved O_2, implying that the evolution of cyanobacteria greatly

predates the rise of oxygen (see review by Farquhar *et al*., 2011 (25)). Fundamentally, however, using O_2 as a proxy for cyanobacteria at such low levels is imperfect and will lead to false-positives, as there are additional sources of O_2 (both biotic and abiotic) that can be important at these concentrations (26–28). Further, many of these elemental proxies have non-unique interpretations and their geochemical cycles are not well understood mechanistically on both short and long timescales (29–31). These proxies can also be impacted by diagenetic and metamorphic processes and studies performed on ancient samples with complex postdepositional histories should be viewed with appropriate caution (e.g., see 29, 32, 33). Sulfur isotope systematics are perhaps the most thoroughly studied, and while the origin of minor isotope mass-anomalous fractionations are not fully understood, the preservation of these effects requires a $pO_2 < 10^{-5.7}$ atm, perhaps closer to 10^{-13} atm (34). Currently, sulfur isotope measurements have constrained the rise of oxygen and minimum age for the origin of cyanobacteria as having occurred between 2.45 and 2.32 Ga (1, 2)—an interval supported by a broad range of geologic evidence (19, 25, 33).

To test these Mn-phototrophy hypotheses, we examined the earliest authigenic Mn deposits paired with several proxies for oxygen to probe the geologic record for evidence of these transitional phototrophs. The behavior of the ancient Mn cycle is useful because it is uniquely sensitive to high redox potential oxidants like O_2: unlike other redox proxies, Mn can only be oxidized by molecular oxygen (or O_2-derived species like superoxide and hydrogen peroxide) or a high potential photosystem (35, 36). Notably,

while Fe was removed from shallow water via oxidation processes in Archean marine environments, the same was not true for Mn (20, 37). In an anoxic Archean world, Mn(II) derived from weathering would have been transported and concentrated in seawater, and, in the absence of high potential oxidants and because Mn does not readily form sulfides, its primary sink would have been as a trace cation constituent of carbonates. Archean (3.5Ga – 2.5Ga) carbonates consequently have much higher Mn contents, up to 1.3% (38) as opposed to Phanerozoic carbonates averaging 30ppm (19). Mn can be further enriched in Archean carbonate host rocks by post-depositional carbonate dissolution and oxidation by oxygenated groundwater and hydrothermal fluids after the rise of oxygen (14, 39). Several small Archean-age manganese ore deposits in Brazil, India, and South Africa developed from carbonate protoliths reflect these processes (14). Conversely, chemical precipitates from seawater like iron formation from Archean deposits typically contain Mn <0.5% (40). Oxidation of aqueous Mn(II) to Mn(III/IV) solids is required to concentrate Mn in iron formation (14). Major Paleoproterozoic Mn deposits, including the ~2.22 Ga Kalahari Manganese Field in South Africa, developed in response to the rise in environmental O_2 (41, 42). Here we report the study of a sedimentary succession underlying and substantially older than the Kalahari deposit but also bearing strong authigenic Mn enrichments. We employ a suite of microscopic and spectroscopic techniques to determine the petrogenesis of Mn-bearing phases, and then turn to several independent redox-sensitive proxies to ascertain the possible paleoenvironmental role of O_2 in generating these deposits. Examining proxies from a micro- to basin-scale improves the identification of post-depositional alteration, and the use of multiple techniques in the

same strata provides an opportunity to address the non-uniqueness common to individual elemental and isotopic proxies.

RESULTS

Manganese oxidation at 2.415 Ga. Two new scientific drill cores through the 2415 ± 6 Ma Koegas Subgroup (conservatively constrained to be <2.43 Ga and >2.22 Ga, see *SI Text*, (43)) were retrieved as a part of the Agouron Drilling Project in Griqualand West, South Africa (Fig. 1, Fig. S1). The Koegas Subgroup contains marine shelf and deltaic sediments deposited on the western margin of the Kaapvaal craton. Observed lithologies include interbedded siliclastics, iron formation with abundant current and wave ripple cross-stratification, and minor carbonates (43). The two cores are aligned across the strike of the basin and capture proximal (GTF01) and distal (GEC01) paleoenvironments, with a higher proportion of iron formation corresponding to the loss of clastic input basinward (Fig. 1). The inboard sections (GTFo1) remain flat-lying and are sub-greenschist in metamorphic grade (44), whereas GEC01 is located on the margin of a younger Paleoproterozoic fold-and-thrust belt (Fig. S1), and was more deeply buried to lower greenschist facies with discrete zones of chlorite formation (44). Well captured by the cores, the Koegas strata contain horizons in iron formation with anomalous Mn concentrations (43, 45), ranging from 1 to 16.6% (weight percent) in bulk (Fig. 1), which is extremely enriched compared to average Archean iron formation concentrations of <0.5% (40). We observed elevated sedimentary Mn concentrations repeatedly throughout both cores in condensed sequence stratigraphic intervals (Fig. 1). This illustrates that

sedimentary Mn concentrations were high in all environments and interpreted as having low relative sedimentation rates (e.g., maximum flooding intervals and delta lobe-switches) regardless of position on the shelf or paleowater depth.

The Mn phases responsible for the enrichments in these rocks are very fine-grained and intimately associated with mixed valence iron-bearing minerals, making their analysis by standard methods challenging. Because textural context is critical to understanding the origin of these phases, we employed a new set of X-ray absorption spectroscopy techniques that provide insight into redox states and coordination environment of Mn across a large range of length scales. In addition to X-ray absorption near edge spectroscopy (XANES) of the Mn K-edge of bulk powders, we used a microprobe technique with 2μm resolution to obtain XANES spectra on small sample domains and construct micro-scale redox maps of ultrathin sections (46, 47, *SI Text)*. We tested these methods on the well-characterized Kalahari Mn Field of the Hotazel Fm, in which Mn is hosted by two phases, braunite ($Mn(III)_6Mn(II)(SiO_4)O_8$) and kutnohorite ($CaMn(II)_{0.7}Mg_{0.3})(CO_3)_2$ (48) (Fig. S3, Fig. S4). The kutnohorite yields a low $\delta^{13}C$ signature (-8.1 to -12.5‰), is found in abundant concretions and laminae, and is interpreted to be secondary and diagenetic in origin from the coupled oxidation of organic carbon and reduction of manganese oxides in sedimentary pore fluids (48, 49), leading to the precipitation of Mn-carbonates:

$$2\ MnO_2 + CH_2O + 2\ H^+ \rightleftharpoons 2\ Mn^{2+} + CO_3^- + 2\ H_2O \quad (1)$$

$$Mn^{2+} + CO_3^{2-} \rightleftharpoons MnCO_3 \quad (2)$$

We acquired XANES spectra of these carbonate concretions and their braunite matrix at a 2μm resolution (Fig. S3). We then used spectral differences between these endmembers to distinguish Mn redox states for each pixel and construct a redox map. A redox map from the Kalahari Mn deposit cleanly differentiates Mn(II) carbonate concretions from the Mn(III+II) braunite matrix (Fig. 2; Fig. S4).

In contrast to the Kalahari Hotazel Formation, XAS measurements and multiple energy redox maps of 2.415 Ga Mn enrichments throughout both cores, which occur in granular and banded iron formation, reveal that the Mn enrichments are spatially heterogeneous and exclusively in a Mn(II) valence state (Fig. 2; Fig. S3*B*). Bulk and point spectra best match kutnohorite and rule out the presence of Mn-oxides [Mn(III) or Mn(IV)] at the ~ 5% abundance level (at any scale) (Fig. S3). We confirmed the localization and heterogeneity of Mn in carbonate phases by energy-dispersive spectroscopy (Fig. 3 *A* and *B*).

Several independent observations reveal that these Mn carbonates in the Koegas subgroup have a secondary, diagenetic origin from reduction of sedimentary Mn oxide phases, described in Eqns. (1) and (2). The Mn mineralization is not associated with post-depositional leaching of carbonate beds or more permeable lithologies like sandstones (Fig. 1). We tested whether later metasomatic fluids (potentially derived from hydrothermal systems in the younger Kalahari Hotazel Formation that occurs ~150km to

the north; Fig. S1) could have introduced the Mn by measuring concentrations in veins and found they had no Mn enrichments (Fig. S5). Rather, the Mn enrichments are stratigraphically restricted to condensed horizons of iron formation, concentrated in authigenic 10-40μm Mn-carbonate crystals that display diagenetic textures (Fig. 3 *A* and *B*; Fig. S6). The C isotopic composition of these Mn-carbonate phases is highly variable and strongly ^{13}C-depleted from values of seawater dissolved inorganic carbon (Fig. 3*C*; Fig. S11, S12). These observations imply that the carbonates were precipitated from pore fluids influenced by the microbial respiration of organic carbon (e.g., Eqn. 1). The Mn and Fe contents of these carbonates, their diagenetic textures, and their carbon isotopic values indicate that these secondary carbonates were formed from reduction of Mn and Fe oxides, a process widely recognized from Archean and Paleoproterozoic iron formations (20, 48) and Mn ore deposits (48). Examples of diagenetic Mn-bearing carbonates produced from reduction of Mn-oxides are well known from Mesozoic and Neogene deep-sea sediments, driven by reactions with Mn oxide phases with sedimentary organic matter, and show very similar isotopic characteristics (49, 50). Together these results indicate the sediments accumulated solid Mn-oxide phases, resulting in precursor sediments enriched with Mn-oxides at the time of deposition, which were subsequently reduced to Mn-carbonate during early diagenesis.

Environmental O_2 levels were very low during Koegas deposition. The oxidation of Mn to form these precursor Mn oxides points to the existence of high potential oxidants in the environment prior to 2.415 Ga. It is notable that although marine

paleoenvironments throughout this basin were capable of producing Mn-oxides, the sedimentary environment was not able to stabilize them, suggesting the lack of O_2 in this environment; were O_2 present in surface sediments, then Mn-oxides could persist because O_2 is a more favorable electron acceptor (51). To further ascertain whether the Mn oxidant was provided by O_2 or a Mn-oxidizing photosystem, we examined the behavior of several independent redox-sensitive proxies. We investigated whether O_2-sensitive detrital grains were present in intercalated Koegas sandstones and whether early diagenetic pyrite in shale lithologies bears mass independent S isotope signals.

We observed detrital pyrite grains in subarkosic sandstone beds throughout the GTF01 core (Fig. 1). These redox-sensitive grains offer a simple and straightforward proxy for environmental O_2 because, in the presence of O_2, pyrite is unstable and undergoes rapid oxidative chemical weathering. Consequently, redox-sensitive detrital grains are common in fluvial and nearshore marine sediments prior to the rise of oxygen (19, 52), and extremely scarce thereafter (19). Physically rounded pyrite grains in these marine sediments (Fig. S7) indicate the lack of O_2 during their weathering, transport, and sedimentation. The detrital origin of these pyrite grains is identified by their rounded, irregular shape, proximity to other dense mineral grains such as zircons and monazites, and in some cases observations of grain-boundary truncations (Fig S7). We confirmed that these grains had a provenance distinct from authigenic pyrite (53) by measuring multiple sulfur isotope ratios from two thin sections using SIMS, finding distinct mass-anomalous fractionations (mean $\Delta^{33}S$: -1.12‰; Table S1) that differ from authigenic

pyrite with mainly zero or positive $\Delta^{33}S$ (discussed below). Redox-sensitive detrital pyrite is thought to be sensitive to environmental O_2 concentrations of approximately $10^{-5.7}$ atm (54).

Multiple sulfur isotope ratios ($\delta^{34}S$ and $\Delta^{33}S$) provide another independent proxy sensitive to very low levels of atmospheric O_2 ($< 10^{-5.7}$ atm (34)), and currently constitute the most established geochemical standard for marking the rise of oxygen (1, 2, 55). In addition to detrital pyrite in the sandstones, Koegas strata contain shale horizons with authigenic sulfide-bearing minerals. However, it is also clear from petrography that these phases record multiple episodes of sulfide mineralization, including euhedral ingrowths and overgrowths, fracture-filling cements, and replacements (Fig. S8, Fig. S9)—requiring careful analysis and interpretation of isotope ratio data. To untangle this history we complimented our bulk SF_6 gas source mass spectrometry analyses with secondary ion mass spectrometry (SIMS), which enabled us to connect multiple sulfur isotope measurements to texture and insight gained from petrography and cross-cutting relationships. The SF_6 and SIMS data overlap and record the same systematics (Fig. 4; Fig. S11, Fig. S12). Altogether the multiple sulfur isotope data reveal two discordant isotopic trends. Pyrites with late textures show a $\Delta^{33}S$ near zero and highly variable and positive $\delta^{34}S$ values, whereas pyrites that lack these late textures show $\Delta^{33}S$ values with clear mass anomalous fractionations and muted $\delta^{34}S$ values—two features characteristic of strata deposited prior to the rise of oxygen (55). These multiple S isotope data imply environmental O_2 concentrations at this time were far less than $10^{-5.7}$ atm (34).

DISCUSSION

The extensive accumulation of manganese-rich deposits ca. 2.415 Ga indicates prevalent Mn oxidation, but independent redox-sensitive proxies (detrital pyrite and anomalous multiple S isotope fractionations) suggest that environmental O_2 concentrations remained very low. The sedimentary Mn concentrations we observe are too high for abiological mechanisms (*SI Text*) and therefore require a biological oxidation mechanism. This is consistent with the idea of transitional Mn-oxidizing phototrophy prior to the rise of cyanobacteria and oxygenic photosynthesis. However, to examine the possibility that O_2 production by cyanobacteria was responsible for our Mn deposits, we considered scenarios wherein the Mn oxides might have been created by reacting with O_2.

Some have postulated the existence of 'oxygen oases' adjacent to cyanobacterial mats prior to the rise of oxygen, in which oxygen production could exceed the vanishingly low global O_2 average (56). The observations of Mn, redox-sensitive detrital grains, and anomalous multiple sulfur isotope fractionations within Koegas Subgroup facies model do not support the existence of such oases in this sedimentary basin. The Mn-enrichments are not uniquely tied to microbial mat lithofacies or a restricted paleoenvironment, but rather are found across the basin, both up and down depositional dip, implying a continuity of process over > 50km of the ocean basin that separates our two cores (Fig. S1). This includes deep-water iron formation facies that accumulated chemical sediment from suspension. Moreover, Mn deposits occur in formations spanning the entire Koegas

Subgroup, over ~230m of stratigraphy in GEC01 and ~210m in GTF01. This repeated sequence stratigraphic occurrence indicates Mn deposition across a broad range of space and time and is not consistent with a transient, restricted mat environment producing O_2. Rather, independent of Mn, all of our observations instead point to its paucity. Shallow water environments with cross-stratified sandstones have repeated occurrences of redox-sensitive detrital grains in every bed examined throughout the stratigraphy. Shales throughout the stratigraphy have pyrite nodules bearing anomalous sulfur isotope fractionations. These proxies are sensitive to O_2 both locally and globally, and strongly suggest that oxygen oases were not responsible for creating the Mn enrichments in the Koegas Subgroup.

It is also important to consider whether the very low levels of O_2 permissible from the different redox proxies might have been sufficient to oxidize Mn, concentrating oxides in Koegas sediments. It was hypothesized that O_2 cycled as a trace gas prior to the rise of oxygen (57), and from a thermodynamic perspective, Mn is sensitive to low levels of oxygen (~ 10^{-10} atm). However it is widely recognized that the abiotic kinetics of Mn^{2+} oxidation by O_2 are extremely slow (58). Biological oxidation using O_2 is notably faster (35, 58), but occurs at rates too slow to explain the enrichments observed here. Calculations of Mn oxidation rates at O_2 concentrations of 2.6 nM–the maximum value allowed by multiple sulfur isotope constraints—yield 0.073 g of oxidized Mn per liter per kyr, or between 0.02% to 0.2% of the total sediment mass depending on sedimentation rate estimations. These calculations use the maximal biological rates, highest possible

dissolved O_2 concentrations, assume conservatively that all Mn-oxides reduced were converted to carbonate phases with no return loss to seawater, and still are insufficient to produce these Mn deposits *(SI Text)*. For these reasons we do not favor O_2 as the oxidant responsible for creating the sedimentary Mn-enrichments we observe. Oxidation rates catalyzed by a photosystem are much faster (59), and consequently we postulate that these Mn deposits were derived from a manganese-based photosynthetic process. Similar to photoferrotrophy proposed for the accumulation of iron in Archean iron formations (60), we interpret the original manganese oxides as products of anoxygenic photobiology, with Mn(II) donating electrons directly to an ancestral reaction center.

The integrated results presented here indicate that the oxidative branch of the manganese cycle was operating prior to 2.415 Ga, but reveal that Mn was not oxidized by O_2. These observations suggest that a transitional photosystem lent the biochemical capability of using Mn as an electron donor, and support a distinct class of hypotheses for the origin of the WOC of PSII that describe single electron photooxidation reactions involving manganese as an evolutionary intermediate in the development of one of biology's greatest achievements—light-driven water oxidation.

METHODS

Bulk element geochemistry was measured using X-ray fluorescence and inductively coupled plasma mass spectrometer (ICP-MS). XAS analyses were generated from monolayer powders or ultra thin sections at SSRL. Thin section samples were examined

by SEM using EDS for elemental mapping. Values of $\delta^{13}C$ and $\delta^{18}O$ for carbonates were measured on a MAT 253 isotope ratio mass spectrometer. Pyrite $\delta^{34}S$ and $\Delta^{33}S$ were measured in bulk at the MIT Stable Isotope Laboratory and *in situ* on a Cameca 7f-GEO. See *SI Text* for additional details on materials and methods.

FOOTNOTES

Abbreviations:

$\delta^{34}S = ([^{34}S/^{32}S_{samp}]/[^{34}S/^{32}S_{std}])-1)1000$

$\delta^{33}S = ([^{33}S/^{32}S_{samp}]/[^{33}S/^{32}S_{std}])-1)1000$

$\Delta^{33}S = 1000(\ln(1+(\delta^{33}S/1000))-0.515(\ln(1+ (\delta^{34}S/1000))$

ACKNOWLEDGEMENTS

We thank James Hemp for useful discussions and valuable manuscript feedback, Yunbin Guan for assistance with the ion microprobe data collection and reduction, Kristin Bergmann for discussions and assistance with sample preparation and analyses, Nic Beukes for helpful comments and assistance in the field, Chi Ma for assistance with SEM and e-probe analyses, Benjamin Kocar and John Bargar for additional help at the synchrotron, and George Rossman, John Eiler, Tim Raub, and John Abelson for helpful discussions and laboratory assistance. We also thank the valuable insights of four anonymous reviewers. Support for this work was provided by the Agouron Institute, NASA Exobiology (W.W.F.), the David and Lucile Packard Foundation (W.W.F.), and the NSF Graduate Research Fellowship program (J.E.J.). Data are available in

supplementary tables. Portions of this research were carried out at the Stanford Synchrotron Radiation Lightsource, a Directorate of SLAC National Accelerator Laboratory and an Office of Science User Facility operated for the U.S. Department of Energy Office of Science by Stanford University. The SSRL Structural Molecular Biology Program is supported by the DOE Office of Biological and Environmental Research, and by the National Institutes of Health, National Institute of General Medical Sciences (including P41GM103393), and the National Center for Research Resources (P41RR001209). The contents of this publication are solely the responsibility of the authors and do not necessarily represent the official views of NIGMS, NCRR, or NIH.

FIGURES

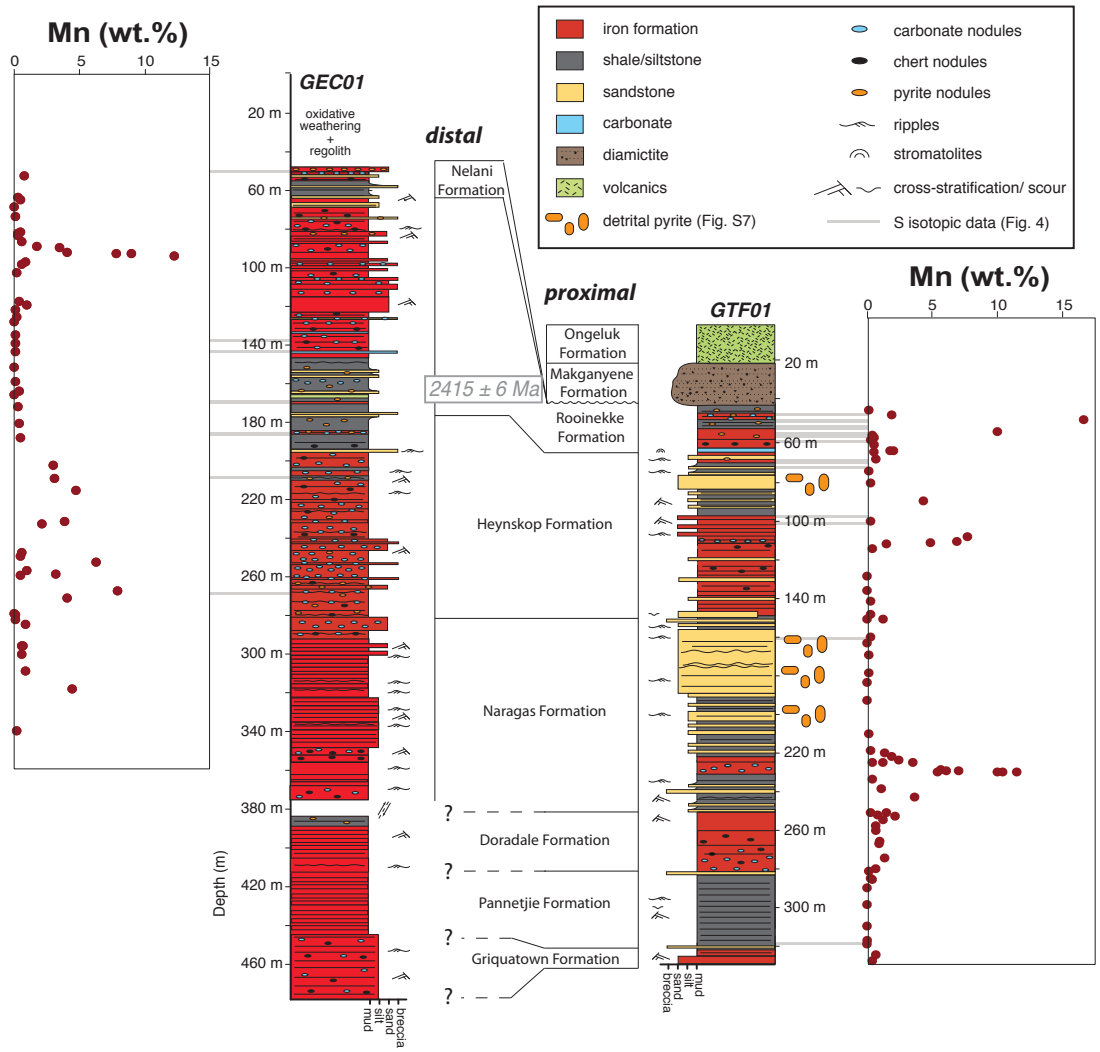

Figure 1. Stratigraphic columns of drill cores GEC01 and GTF01 showing horizons of Mn-enrichments in Agouron drill cores GEC01 and GTF01. Mn abundances were determined by X-ray fluorescence and inductively coupled plasma mass spectrometry. Note the locations of clastic subunits rich in detrital pyrite grains in GTF01 (Fig. S7) and measurements of multiple sulfur isotopes (Fig. 4, Fig. S11, Fig. S12).

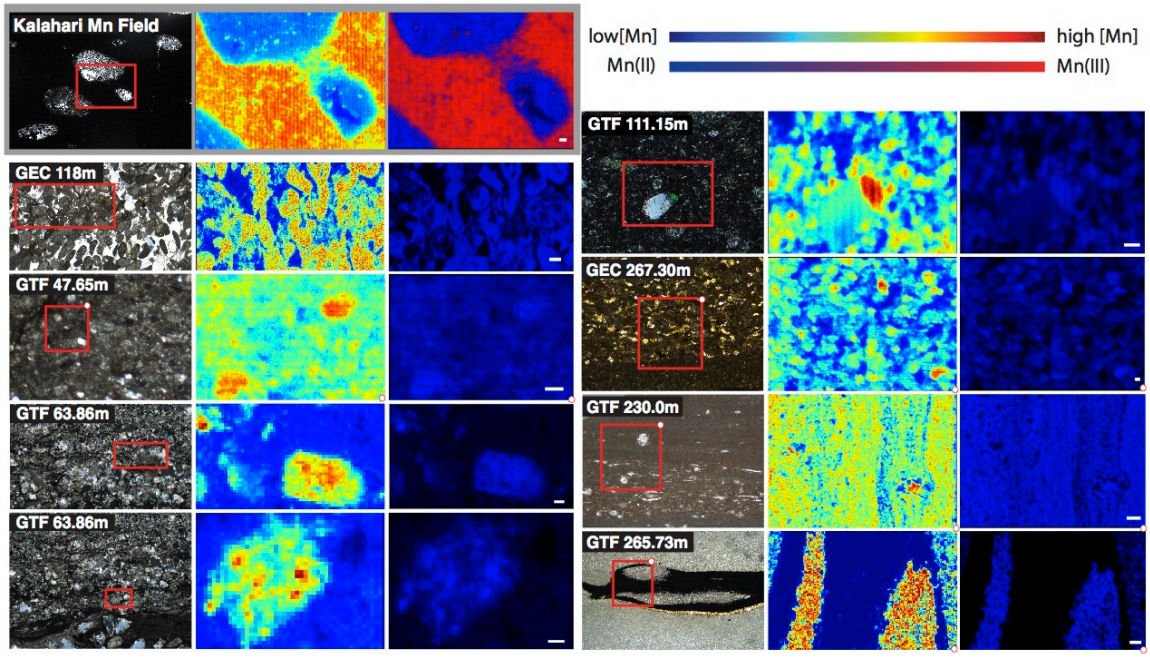

Figure 2. Transmitted light photomicrographs (left panel), Mn concentration maps (middle panel), and Mn redox maps (right panel). Red box inset with small white corner circle highlights the location and orientation of the concentration and redox maps. The X-ray microprobe technique is illustrated on a sample of the ~2.2 Ga Kalahari Mn Field (grey shading), containing braunite and kutnohorite (Fig. S3, Fig. S4). The remaining samples capture the Mn-rich samples from carbonate-rich granular and banded iron formation of the Rooinekke, Heynskop, and Naragas Formations, and reveal exclusively Mn(II)-bearing phases. Scale bars are 20µm except GEC 118m and GTF 230m where they are 100µm. Manganese concentration is in µg/cm^2 and on individual scales to highlight within sample heterogeneity: Kalahari (0 to 1500); GEC 118 (0 to 50); GTF 47.65 (0 to 400); GTF 63.86 (0 to 200); GTF 111.15 (0 to 1000); GEC 267.30 (0 to 1000); GTF 230 (0 to 500); GTF 265.73 (0 to 50).

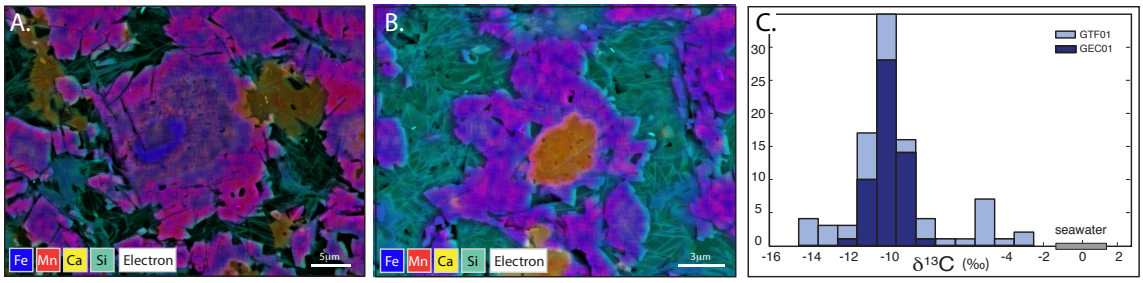

Figure 3. (A) and (B) Backscatter electron images with overlying electron dispersive spectroscopy elemental maps show the variable compositions and diagenetic textures of the Mn-bearing carbonates with Mn shown in red, Fe shown in blue, Ca shown in yellow, and Si shown in teal. (C) Histogram of $\delta^{13}C$ values (in permill VPDB) from Mn-rich carbonates in GTF01 and GEC01 cores. Grey bar denotes estimated (61, 62) seawater dissolved inorganic carbon $\delta^{13}C$.

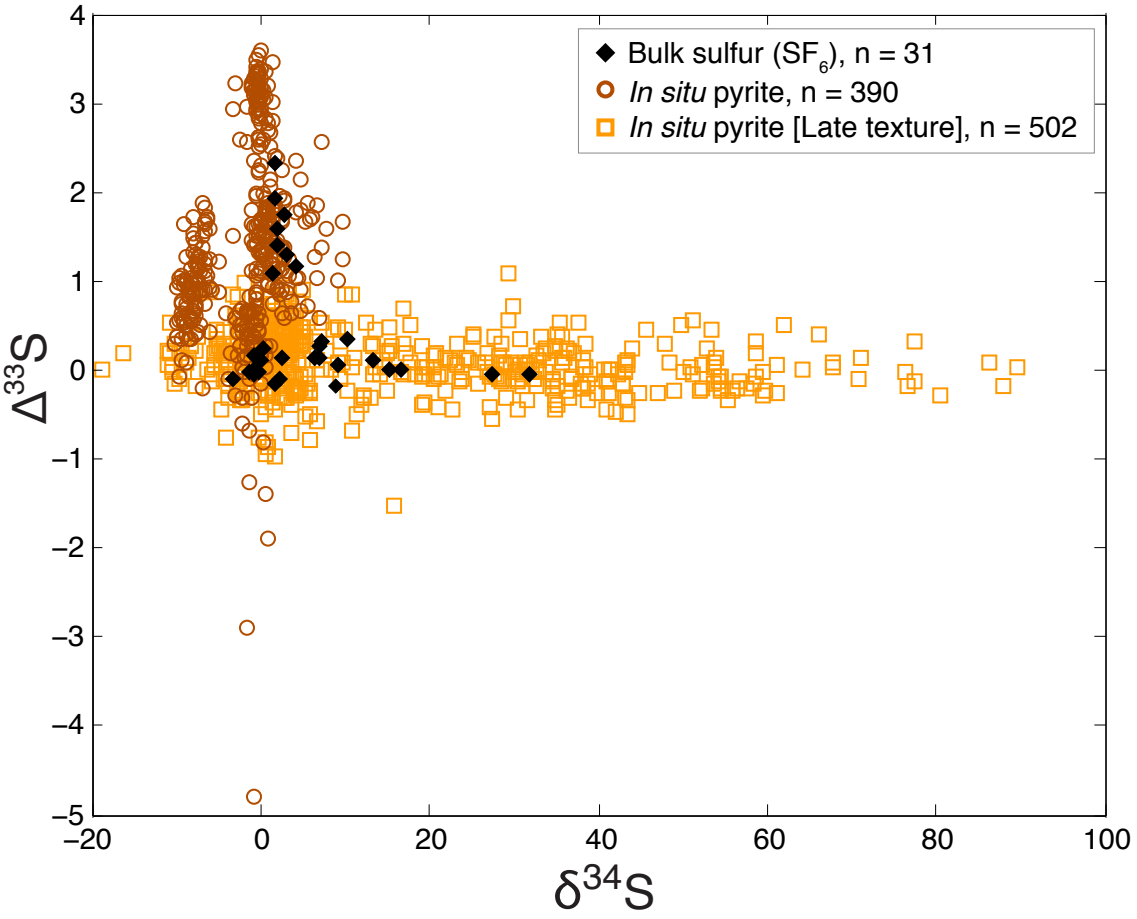

Figure 4. Multiple sulfur isotope ratio data from GTF01 and GEC01 samples (in permill VCDT). SIMS isotope data is further categorized based on petrographic texture (e.g., Fig. S8, Fig. S10). Late pyrites (orange squares) form an array with enriched $\delta^{34}S$ values and $\Delta^{33}S$ near zero and record significant closed system fractionations and perhaps thermochemical sulfate reduction from late fluids during burial metamorphism and late diagenesis. The 2σ uncertainties for the SF_6 data are 0.26‰ or better and better than 0.4‰ for SIMS data. The large deviations of $\Delta^{33}S$ from zero for the *in situ* pyrite (brown circles) is characteristic of Archean and early Paleoproterozoic-age rocks and is indicative of an anoxic atmosphere.

REFERENCES CITED

1. Bekker A et al. (2004) Dating the rise of atmospheric oxygen. *Nature* 427:117–120.

2. Guo Q et al. (2009) Reconstructing Earth's Surface Oxidation Across the Archean-Proterozoic Transition. *Geology* 37:399–402.

3. Xiong J, Fischer WM, Inoue K, Nakahara M, Bauer CE (2000) Molecular Evidence for the Early Evolution of Photosynthesis. *Science* 289:1724–1730.

4. Williamson A, Conlan B, Hillier W, Wydrzynski T (2011) The evolution of Photosystem II: insights into the past and future. *Photosyn Res* 107:71–86.

5. Ferreira KN, Iverson TM, Maghlaoui K, Barber J, Iwata S (2004) Architecture of the photosynthetic oxygen-evolving center. *Science* 303:1831–1838.

6. Umena Y, Kawakami K, Shen J-R, Kamiya N (2011) Crystal structure of oxygen-evolving photosystem II at a resolution of 1.9Å. *Nature* 473:55–60.

7. McEvoy JP, Brudvig GW (2006) Water-Splitting Chemistry of Photosystem II. *Chem Rev* 106:4455–4483.

8. Olson JM (1970) The Evolution of Photosynthesis. *Science* 168:438–446.

9. Navarro-González R, McKay CP, Mvondo DN (2001) A possible nitrogen crisis for Archaean life due to reduced nitrogen fixation by lightning. *Nature* 412:61–64.

10. Blankenship RE, Hartman H (1998) The origin and evolution of oxygenic photosynthesis. *Trends in Biochemical Sciences* 23:94–97.

11. Sauer K, Yachandra VK (2002) A possible evolutionary origin for the Mn4 cluster of the photosynthetic water oxidation complex from natural MnO2 precipitates in the early ocean. *Proc Natl Acad Sci U S A* 99:8631–8636.

12. Russell M, Allen J, James M-W (2008) in *Photosynthesis. Energy from the Sun*, eds Allen J, Gantt E, Golbeck J, Osmond B (Springer Netherlands), pp 1187–1192. Available at: http://dx.doi.org/10.1007/978-1-4020-6709-9_259.

13. Roy S (1997) in *Manganese Mineralization: Geochemistry and Mineralogy of Terrestrial and Marine Deposits*, Geological Society Special Publication., eds Nicholson K, Hein JR, Buhn B, Dasgupta S, pp 5–27.

14. Roy S (2006) Sedimentary manganese metallogenesis in response to the evolution of the Earth system. *Earth-Science Reviews* 77:273–305.

15. Tamura N, Cheniae G (1987) Photoactivation of the water-oxidizing complex in Photosystem II membranes depleted of Mn and extrinsic proteins. I. Biochemical and kinetic characterization. *Biochimica et Biophysica Acta (BBA) - Bioenergetics* 890:179–194.

16. Zubay G (1996) *Origins of Life on the Earth and in the Cosmos* (Academic Press, San Diego). 2nd Ed.

17. Dismukes GC et al. (2001) The origin of atmospheric oxygen on Earth: The innovation of oxygenic photosynthesis. *PNAS* 98:2170–2175.

18. Allen JF, Martin W (2007) Evolutionary biology: Out of thin air. *Nature* 445:610–612.

19. Holland HD (1984) *The Chemical Evolution of the Atmosphere and Oceans* (Princeton University Press).

20. Fischer WW, Knoll AH (2009) An Iron Shuttle for Deepwater Silica in Late Archean and Early Paleoproterozoic Iron Formation. *Geological Society of America Bulletin* 121:222–235.

21. Brocks JJ, Logan GA, Buick R, Summons RE (1999) Archean Molecular Fossils and the Early Rise of Eukaryotes. *Science* 285:1033–1036.

22. Rasmussen B, Fletcher IR, Brocks JJ, Kilburn MR (2008) Reassessing the first appearance of eukaryotes and cyanobacteria. *Nature* 455:1101–1104.

23. Welander PV, Coleman ML, Sessions AL, Summons RE, Newman DK (2010) Identification of a methylase required for 2-methylhopanoid production and implications for the interpretation of sedimentary hopanes. *PNAS* 107:8537–8542.

24. Rashby SE, Sessions AL, Summons RE, Newman DK (2007) Biosynthesis of 2-methylbacteriohopanepolyols by an anoxygenic phototroph. *PNAS* 104:15099–15104.

25. Farquhar J, Zerkle AL, Bekker A (2011) Geological constraints on the origin of oxygenic photosynthesis. *Photosyn Res* 107:11–36.

26. Haqq-Misra J, Kasting JF, Lee S (2011) Availability of O2 and H2O2 on Pre-Photosynthetic Earth. *Astrobiology* 11:293–302.

27. Liang M-C, Hartman H, Kopp RE, Kirschvink JL, Yung YL (2006) Production of hydrogen peroxide in the atmosphere of a Snowball Earth and the origin of oxygenic photosynthesis. *Proc Natl Acad Sci USA* 103:18896–18899.

28. Ettwig KF et al. (2010) Nitrite-driven anaerobic methane oxidation by oxygenic bacteria. *Nature* 464:543–548.

29. Morford JL, Martin WR, Carney CM (2012) Rhenium geochemical cycling: Insights from continental margins. *Chemical Geology* 324–325:73–86.

30. Helz GR, Bura-Nakić E, Mikac N, Ciglenečki I (2011) New model for molybdenum behavior in euxinic waters. *Chemical Geology* 284:323–332.

31. Nägler TF, Neubert N, Böttcher ME, Dellwig O, Schnetger B (2011) Molybdenum isotope fractionation in pelagic euxinia: Evidence from the modern Black and Baltic Seas. *Chemical Geology* 289:1–11.

32. Scheiderich K, Zerkle AL, Helz GR, Farquhar J, Walker RJ (2010) Molybdenum isotope, multiple sulfur isotope, and redox-sensitive element behavior in early Pleistocene Mediterranean sapropels. *Chemical Geology* 279:134–144.

33. Pufahl PK, Hiatt EE (2012) Oxygenation of the Earth's atmosphere–ocean system: A review of physical and chemical sedimentologic responses. *Marine and Petroleum Geology* 32:1–20.

34. Pavlov AA, Kasting JF (2002) Mass-Independent Fractionation of Sulfur Isotopes in Archean Sediments: Strong Evidence for an Anoxic Archean Atmosphere. *Astrobiology* 2:27–41.

35. Clement BG, Luther III GW, Tebo BM (2009) Rapid, oxygen-dependent microbial Mn(II) oxidation kinetics at sub-micromolar oxygen concentrations in the Black Sea suboxic zone. *Geochimica et Cosmochimica Acta* 73:1878–1889.

36. Kopp RE, Kirschvink JL, Hilburn IA, Nash CZ (2005) The Paleoproterozoic snowball Earth: A climate disaster triggered by the evolution of oxygenic photosynthesis. *Proceedings of the National Academy of Sciences* 102:11131–11136.

37. Beukes N, Klein C (1992) in *The Proterozoic Biosphere: A Multidisciplinary Study*, eds Schopf JW, Klein C (Cambridge University Press).

38. Komiya T et al. (2008) Evolution of the composition of seawater through geologic time, and its influence on the evolution of life. *Gondwana Research* 14:159–174.

39. Varentsov IM (1996) *Manganese Ores of Supergene Zone: Geochemistry of Formation* (Kluwer Academic Publishers, Dordrecht, The Netherlands).

40. Klein C (2005) Some Precambrian Banded Iron-Formations (BIFs) from Around the World: Their Age, Geologic Setting, Mineralogy, Metamorphism, Geochemistry, and Origins. *American Mineralogist* 90:1473–1499.

41. Kirschvink JL et al. (2000) Paleoproterozoic snowball Earth: Extreme climatic and geochemical global change and its biological consequences. *PNAS* 97:1400–1405.

42. Schissel D, Aro P (1992) The Major Early Proterozoic Sedimentary Iron and Manganese Deposits and Their Tectonic Setting. *Economic Geology* 87:1367–1374.

43. Schröder S, Bedorf D, Beukes NJ, Gutzmer J (2011) From BIF to red beds: Sedimentology and sequence stratigraphy of the Paleoproterozoic Koegas Subgroup (South Africa). *Sedimentary Geology* 236:25–44.

44. Miyano T, Beukes NJ (1984) Phase relations of stilpnomelane, ferri-annite, and riebeckite in very low-grade metamorphosed iron-formations. *South African Journal of Geology* 87:111–124.

45. Beukes NJ, Gutzmer J (2008) in *Banded Iron Formation-Related High-Grade Ore*, eds Hagemann S, Rosiere C, Gutzmer J, Beukes N, pp 5–47.

46. Webb SM (2011) The MicroAnalysis Toolkit: X-ray Fluorescence Image Processing Software. *AIP Conference Proceedings* 1365:196–199.

47. Mayhew LE, Webb SM, Templeton AS (2011) Microscale imaging and identification of Fe speciation and distribution during fluid-mineral reactions under highly reducing conditions. *Environ Sci Technol* 45:4468–4474.

48. Tsikos H, Beukes NJ, Moore JM, Harris C (2003) Deposition, Diagenesis, and Secondary Enrichment of Metals in the Paleoproterozoic Hotazel Iron Formation, Kalahari Manganese Field, South Africa. *Economic Geology* 98:1449–1462.

49. Okita PM, Maynard JB, Spiker EC, Force ER (1988) Isotopic evidence for organic matter oxidation by manganese reduction in the formation of stratiform manganese carbonate ore. *Geochimica et Cosmochimica Acta* 52:2679–2685.

50. Matsumoto R (1992) in *Proceedings of the Ocean Drilling Program, Scientific Results*, eds Pisciotto KA, Ingle JC Jr, von Breymann MT, Barron J (Ocean Drilling Program, College Station, TX), pp 75–98. Available at: doi:10.2973/odp.proc.sr.127128-1.119.1992.

51. Froelich PN et al. (1979) Early oxidation of organic matter in pelagic sediments of the eastern equatorial Atlantic: suboxic diagenesis. *Geochimica et Cosmochimica Acta* 43:1075–1090.

52. Rasmussen B, Buick R (1999) Redox State of the Archean Atmosphere: Evidence from Detrital Heavy Minerals in Ca. 3250–2750 Ma Sandstones from the Pilbara Craton, Australia. *Geology* 27:115–118.

53. Hofmann A, Bekker A, Rouxel O, Rumble D, Master S (2009) Multiple sulphur and iron isotope composition of detrital pyrite in Archaean sedimentary rocks: A new tool for provenance analysis. *Earth and Planetary Science Letters* 286:436–445.

54. Anbar AD et al. (2007) A Whiff of Oxygen Before the Great Oxidation Event? *Science* 317:1903–1906.

55. Farquhar J, Bao H, Thiemens M (2000) Atmospheric Influence of Earth's Earliest Sulfur Cycle. *Science* 289:756–758.

56. Kasting JF, Holland HD, Kump LR (1992) in *The Proterozoic Biosphere: A Multidisciplinary Study*, eds Schopf WJ, Klein C (Cambridge University Press, Cambridge, UK), pp 1185–1188.

57. Waldbauer JR, Newman DK, Summons RE (2011) Microaerobic steroid biosynthesis and the molecular fossil record of Archean life. *PNAS* 108:13409–13414.

58. Morgan JJ (2005) Kinetics of reaction between O2 and Mn(II) species in aqueous solutions. *Geochimica et Cosmochimica Acta* 69:35–48.

59. Büchel C et al. (1999) Photoassembly of the Manganese Cluster and Oxygen Evolution from Monomeric and Dimeric CP47 Reaction Center Photosystem II Complexes. *PNAS* 96:14288–14293.

60. Konhauser KO et al. (2002) Could bacteria have formed the Precambrian banded iron formations? *Geology* 30:1079–1082.

61. Bekker A et al. (2001) Chemostratigraphy of the Paleoproterozoic Duitschland Formation, South Africa: Implications for Coupled Climate Change and Carbon Cycling. *Am J Sci* 301:261–285.

62. Fischer WW et al. (2009) Isotopic constraints on the Late Archean carbon cycle from the Transvaal Supergroup along the western margin of the Kaapvaal Craton, South Africa. *Precambrian Research* 169:15–27.

SUPPORTING INFORMATION

Sample collection. GEC01 and GTF01 cores were drilled in the Northern Cape Province of South Africa as part of a second phase of the South African Agouron Drilling Project. These two cores capture the Koegas Subgroup of the Ghaap Group and a portion of the overlying Postmasburg Group (Fig. S1). The Koegas Subgroup overlies the Asbestos Hills Subgroup, composed of the Kuruman and Griquatown formations. The upper Kuruman formation has ash beds dated by U-Pb SHRIMP on zircons to 2460±5 Ma (1) and the Griquatown Formation has zircons dated by U-Pb SHRIMP to 2431±31 Ma from published conference proceedings (2, 3). Overlying the Koegas Subgroup is the Makganyene Formation (a glaciogenic unit deposited on top of a substantial regional unconformity, (4–6)) and the Ongeluk Formation, which has been dated by whole-rock Pb-Pb isochron to 2238±90 Ma (7, 8) and refined in a later study by whole-rock Pb-Pb to 2222±12 Ma (9). Zircons from an ash bed in the Rooinekke Formation of the Koegas Subgroup were dated by SHRIMP U-Pb to 2415±6 Ma in a technical report (5, 10), which currently constitutes the best age constraint for the Koegas Subgroup (5, 6, 11–13). Cores were slabbed and logged and half were sent to the California Institute of Technology with the other half archived at the Council for Geoscience in South Africa. Details of the sedimentary geology and bulk geochemistry can be found in Schröder et al (5). Subsamples for petrographic and geochemical analysis were collected from the cores using non-magnetic blades and bit on a trim saw and drill press, respectively.

Sample preparation and bulk element geochemistry. A preliminary dataset for the major, minor, and trace element geochemistry was acquired at the SPECTRAU analytical facility at the University of Johannesburg (5). Wavelength-dispersive X-ray fluorescence analyses (XRF) were used on the lithium borate ($Li_2B_4O_7$-$LiBO_2$) fused glass bleads on a Philips Magix Pro Spectrometer. Elemental composition was determined with precision better than 0.5% and accuracy better than ±5% for most elements except iron, which was better than ±10%. A second set of core subsamples was analyzed for bulk chemistry in the Activation Laboratories, Ancaster, Ontario. Chips of core (0.5 g each) were pulverized and digested in aqua regia in a microprocessor controlled digestion block at 90ºC for 2 hours. After diluting the resultant solution, 28 elements were analyzed by ICP/MS using a Perkin Elmer SCIEX ELAN 6000, 6100, or 9000 ICP/MS. Digestion duplicates were analyzed every 15 samples. An in-house control was run every 33 samples and blank and digested standards were run every 68 samples and instrument was recalibrated. Each batch of samples is bracketed by international reference materials, and a duplicate and internal control standards are analyzed every 10 samples. Some silicates, oxides, and resistant materials such as zircon and monazite were not totally dissolved. For more precision on highly Mn-concentrated samples, a lithium metaborate/tetraborate fusion-ICP method was used. These samples were run with replicates, a method reagent blank, and certified reference material. Samples were fused in an induction furnace after mixing with lithium metaborate and lithium tetraborate. The molten melt was added to a 5% nitric acid solution with an internal standard, and mixed ~30 minutes until completely dissolved. The samples were then run for manganese concentration on a combination

simultaneous Thermo Jarrell-Ash ENVIRO II ICP or a sequential Varian Vista 735 ICP. The instrument is calibrated using seven certified reference materials. Data are available in Table S1.

Small samples for bulk XAS were chosen from Mn-rich intervals of both cores as well as several samples from strata with conspicuous but lower Mn concentrations (see Table S1). A micro-rotary drill with a 1mm bit was employed to produce coarse powders of all visible textures, producing ~100-200mg of powder. These samples were loaded into small glass vials and then transferred to an anaerobic chamber. In this chamber, a ceramic mortar and pestle was used to further grind this powder into a very fine, homogenous mixture. The powder was then spread evenly onto monolayers of *Scotch* tape to produce approximately 6 to 14 layers, depending on Mn concentration. These monolayer tape samples were then stored in heat-sealed mylar bags, except for one duplicate which was prepared and stored in air. The use of anaerobic glove box and vacuum bags were used to prevent any oxidation of reduced Mn in the samples. However, these extra steps were unnecessary, as the XAS spectra of the same sample prepared both anaerobically and aerobically are identical (Fig. S2). This result is consistent with theory and measurements of abiotic Mn oxidation by O_2—a process that is strongly kinetically limited and proceeds very slowly in solution (14) and essentially does not occur in dry air.

Carbonate nodules and ankerite-dominated intervals were targeted for carbonate sampling using a micro-rotary drill with a 1mm bit. These microsampled powders were stored in glass vials.

Slabs and rounds were prepared from desired strata for analyses on the Scanning Electron Microscope (SEM), the Electron Microprobe (E-probe), on beam line (BL) 10-2 and 2-3 at Stanford Synchrotron Radiation Lightsource, and on the Secondary Ion Mass Spectrometry instrument (SIMS). Slabs were cut using a rock saw and rounds were made using a 1-inch drill press, targeting desired sections. Billets and rounds of approximately 5mm were made into thin sections by High Mesa Petrographics or Spectrum Petrographics, and carefully polished to obtain a microprobe quality surface. For use on the SEM and E-probe, returned thin sections were subsequently carbon coated with 7-15 nm of graphite using a Cressington Carbon Coater. Before analysis using the SIMS, thin sections were sputter coated with gold (30 nm) using a Cressington Sputter Coater. Ultrathin sections (~10μm) were made for XAS to minimize the amount of sample volume felt by the X-ray beam. The Mn concentration of the thin section glass is below the detection limit of our analyses.

Samples adjacent to sections prepared for *in situ* (SIMS) analyses were targeted for bulk sulfur measurements. These were removed from the core and cubed using a rock saw. They were then powdered using an SPEX 8510 Shatterbox to yield approximately 2 to 5g of sample. Extremely ^{34}S-enriched pyrite cements (as shown by *in situ* measurements,

Fig. 4, Fig. S10, Table S3) from fracture filling cements were also sampled using a micro-rotary drill for comparison to *in situ* measurements (yielding 1.2 to 2.1 mg, Table S3 labeled with '^'). Additionally, an in-house pyrite standard used for *in situ* measurements was sub-sampled for analyses to assay standard homogeneity.

Bulk powder X-ray absorption spectroscopy. Beam line 4-1 at SSRL was used to analyze 16 samples for bulk manganese oxidation state and coordination environment. A Silicon 220 Φ = 90 crystal was used and X-ray absorption spectra (XAS) was collected on a Lytle detector for fluorescence and on an absorption detector for transmission spectra. A collimating mirror was used to help reduce harmonics in the beam, and a potassium permanganate ($KMn(VII)O_4$) standard was used for calibration. Duplicates were run on all spectra collected for X-ray Absorption Near Edge Spectroscopy (XANES) scanning from 6310 eV to 7108 eV. Representative samples were targeted for X-ray Absorption Fine Structure (XAFS) with ~4 repeats for higher Mn concentrations and ~10 repeats for lower Mn-bearing samples scanning from 6310 eV to 7223 eV.

XAS Mapping. Beam line 10-2 at SSRL was used to analyze 12 samples for coarse resolution mapping. Polished thin sections (rounds or rectangular) were analyzed at three energies determined to distinguish redox states: 6551 eV, 6562 eV, and 6572 eV. Maps were generated by collecting the X-ray fluorescence using a Vortex FII International Silicon drift detector on ~80μm x 80μm pixels (focused by capillary optics), which were rastered over the sections. Regions of interest were subsequently mapped in higher

resolution on BL 2-3 at SSRL at ~10μm resolution (with a 2μm beam using Kirkpatrick Baez mirrors for focusing) on a Vortex FII International Silicon drift detector using 4 redox-distinctive energies determined from braunite and kutnohorite from the Kalahari Manganese Field (Fig. S3, Fig. S4), using the maximal normalized fluorescence differences between these endmembers as targets for redox-distinguishing energies (Fig. S4). The braunite spectra were chosen as a representative end member, as they capture the most oxidized (though still mixed valence) phase found in Mn-rich sedimentary rocks of similar diagenetic and metamorphic grade like nearby Kalahari Manganese Field. We chose kutnohorite as the reduced endmember for our multiple energy maps, as our bulk XAS spectra best matched the Kalahari kutnohorite (Fig. S3). The redox-distinguishing energies chosen for high-resolution maps were 6542 eV, 6551 eV, 6560-62 eV, 6572-73 eV, and sometimes 6546 eV, 6548 eV, 6558 eV, and 6568 eV (Fig. S3). To rule out the presence of even small domains of Mn oxide-bearing phases a multiple energy map at ~2μm resolution was also generated for most of the samples (Fig. 2).

Multiple energy maps were analyzed using the MicroAnalysis Toolkit software (15). Maps of each energy were imported into one master file, thereby having a set of distinctive absorptions at several energies for every map pixel (i.e., a "mini-XANES spectrum" (15)). These pixels were then analyzed using a non-negative linear-least squares fit of the data to the two end member spectra, an Mn(II)-bearing carbonate and an oxidized Mn(III)-bearing braunite from the Kalahari Mn field using the MicroAnalysis Toolkit fitting function. Normalized intensity of the absorption spectra of the two end

members was determined for the energies measured, and then each pixel was fit to the composition of each standard. Subsequent confirmation of the fit is found by measuring XANES spectra at pixels identified as distinct by a principal component analysis of the multiple energies (15, 16). Fitted pixels were all set to the same scale, 0 to 1500 counts for kutnohorite (Mn-bearing carbonate) and 0 to 4000 counts for braunite. Fitted results agree within 5 percent (15) and all full XANES spectra collected at specific 2x2μm points support the fitted-pixel redox maps.

To quantify Mn concentration, the highest energy map was used (6572 eV or 6573 eV). The manganese abundance was collected in counts, which were converted to units of $\mu g/cm^2$ using a map made at the same energy and under the same conditions (incident monochromator energy and detector distance) of an Mn foil, made from Mn deposited on a mylar film at a concentration of 47.1 $\mu g/cm^2$. After removing edge effects of the standard map, a QuantFile of the standard was created to calibrate against the data files. Scales were then adjusted to the closest multiple of 50 for comparative purposes (scales range from 50 to 1500 in order to best show small-scale variations of Mn).

SEM/E-probe. A Zeiss 1550VP Field Emission Scanning Electron Microscope equipped with an Oxford INCA Energy 300 X-ray Energy Dispersive Spectrometer (EDS) system housed in the Geological and Planetary Sciences (GPS) Division Analytical Facility was used for all analyses. High-resolution images were taken in backscatter electron imaging mode to enhance compositional contrast. EDS measurements of x-ray fluorescence were

made mainly on points (see Fig. S3) but also as x-ray fluorescence maps (Fig. 3). Quantitative elemental analysis provides relative accuracy of better than 5%. These capabilities were used to identify detrital minerals such as pyrite and zircon, in order to examine pyrite nodules and fracture fills examined on the SIMS, and to investigate the textural complexity of samples from GTF01, GEC01, and from the Kalahari Mn field.

Other measurements were made on a JEOL JXA-8200 Advanced Electron Probe Micro-analyzer (E-probe) equipped with five wavelength dispersive X-ray spectrometers (WDS), tungsten and LaB_6 electron sources, and a detection limit of several hundred ppm. It has an accuracy as good as 1-2% and the precision on pyrite is 0.2% (S) and 0.4% (Fe). The detection limit for manganese was 300ppm, and all samples identified as pyrite phase (FeS_2) were below the Mn detection limit. A late-stage fracture with discontinuous pyrite mineralization (characterized by heavy $\delta^{34}S$ values) was examined on the E-probe and the concentration of manganese was measured from spots throughout the mineralized fracture. The Mn concentration was below detection limit for 40 measurements and below 0.1% of the total concentration for the remaining measurements, discounting 3 outliers (Fig. S5). These outliers were measurements made on non-pyrite but instead captured (partially or totally) some of the Mn-bearing matrix. Even including the outliers, the total Mn percentage is less than 0.5% in all points measured, highlighting the lack of Mn delivery from metasomatic fluids.

Carbonate C and O isotopic analysis. Carbonate samples were measured for their carbon isotopic distribution at the University of Michigan Stable Isotope Laboratory. Samples are heated to 200ºC for one hour, removing any volatile contaminants and water. Samples are then reacted at 77 ± 1ºC with anhydrous phosphoric acid for 22 minutes in individual borosilicate reaction vessels in a Finnigan MAT Kiel IV preparation device. This is directly coupled to the inlet of a Finnigan MAT 253 triple collector isotope ratio mass spectrometer, which measures isotopic measurements calibrated against NBS 18 and NBS 19. Data are reported in delta notation (‰) relative to VPDB and measured precision is better than 0.1‰ as assessed by multiple analyses of a variety of carbonate standards. The data is available in Table S2. Estimates for the carbon isotopic composition of dissolved inorganic carbonate (DIC) during this time period were derived from Bekker et al. (17) and Fischer et al. (18) (Fig. 3).

Bulk S isotope analysis by SF_6 gas source mass spectrometry. At the MIT Stable Isotope Laboratory, pyrite sulfur was extracted from powdered rock samples by chromium chloride reduction following a method modified from (*61*). A 1M $CrCl_3$ solution was reduced using zinc metal (4g zinc/40mL of $CrCl_2$). Sample powders (1.5g to 5g) were added to a round bottom flask connected to a condenser with a sidearm to allow N_2 to flow through. The condenser was connected to a water trap filled with 60-70 mL of DI H_2O for condensed phases and a trap containing ~50 mL of zinc acetate. Approximately 30 mL of chromium chloride solution was added to the sample powders after flushing and then heated to boiling for 2-3 hours to drive off H_2S and ultimately

precipitate ZnS. Once the reaction has completed, silver nitrate was added (5mL) to react with the zinc sulfide and form precipitated silver sulfide (Ag_2S). The precipitates were washed with NH_4OH (to remove any silver hydride) and ultrapure DI water and dried. The silver sulfide was then reacted with F_2 at 300°C. Reacted SF_6 was transferred via liquid nitrogen cold traps, removing any extraneous F_2, and purified by means of a gas chromatograph. The SF_6 was then fed into a Thermo 253 dual-inlet mass spectrometer, where the isotopes ratios sulfur isotopes (^{32}S ^{33}S ^{34}S ^{36}S) were measured against in-house standards. This method offers a precision of 0.26, 0.014 and 0.19 ‰ (2σ) for $\delta^{34}S$, $\Delta^{33}S$ and $\Delta^{36}S$ values based on multiple measurements of reference materials (IAEA S-1: $\delta^{34}S$ -1.34±0.13, $\Delta^{33}S$ 0.10±0.007 and $\Delta^{36}S$ -0.57±0.10, IAEA S-2: $\delta^{34}S$ 21.18±0.13, $\Delta^{33}S$ 0.043±0.005 and $\Delta^{36}S$ -0.16±0.05, IAEA S-3: $\delta^{34}S$ -33.54±0.13, $\Delta^{33}S$ 0.091±0.020 and $\Delta^{36}S$ -0.58±0.11). The data are reported in delta notation (‰) with respect to VCDT, and are reported in Table S3.

***In situ* S isotope analysis by secondary ion mass spectrometry.** We employed a Cameca 7f-GEO, a pseudo multi-collector SIMS instrument with three separate collectors that measure different ions in rapid succession by dynamic peak hopping, housed within the Center for Microanalysis at the California Institute of Technology. The instrument was operated at a primary beam current of ~ 3nA with a spot size of ~25μm. We measured ^{32}S, ^{33}S, and ^{34}S with a MRP of ~ 4000 to separate ^{33}S from ^{32}SH, and typically achieve ~ 10^9 counts s^{-1} of ^{32}S, and ~ 10^8 and ~ 10^7 counts s^{-1} for ^{34}S and ^{33}S, respectively. Sample unknowns were bracketed by measurements of an inhouse pyrite

standard ($\delta^{34}S$ 1.024‰, $\delta^{33}S$ 0.608‰), co-mounted in epoxy close to the regions of the sample of interest and polished to obtain the same flat analytical surface. Data was corrected for Faraday cup yield differences (^{32}S was collected on Faraday cup 1 and ^{33}S and ^{34}S are collected on Faraday cup 2) and instrumental mass fractionation of isotopes. External precision (defined as the standard deviation of multiple adjacent measurements of standards) is typically better than $\delta^{34}S$ = 0.4‰, $\delta^{33}S$ = 0.3‰, and $\Delta^{33}S$ = 0.15‰. (For measurements on detrital pyrite grains, precision is similar for $\Delta^{33}S$ but is up to 1.3‰ for $\delta^{34}S$, as standards were not on same mount adjacent to pyrite.) The data are reported in delta notation in permill with respect to VCDT, and is available in Table S3.

Kinetics of manganese oxidation by O_2. Mn(II) oxidation by the low levels of molecular oxygen allowable by our independent redox proxies does not explain the enrichments observed in Koegas strata. While thermodynamics dictate that molecular oxygen will oxidize Mn(II) at far less than 10^{-10} atm, oxidation reactions by O_2 are strongly kinetically limited (14, 19). Even at modern oxygen levels, abiological manganese oxidation is exceedingly slow—kinetic limitations result in an Mn(II) half life of 30 days for oxide-stimulated oxidation and 400 days for a homogenous solution with $Mn^{2+}_{(aq)}$ and O_2 (under a 0.21 atm pO_2 atmosphere) (14). Considering that molecular oxygen produced in the surface ocean will reside for an average of approximately 17 days before escaping to the atmosphere (20), abiological mechanisms are not rapid enough to produce the volume of manganese we observe.

Biological manganese oxidation (using O_2) proceeds more rapidly and is thought to be the main mechanism for Mn oxidation in modern environments — under today's atmosphere, Mn(II) has a half life of 10 hours (14). This process is most efficient at enzyme saturation, at a range of 0.87 to 11μM of dissolved O_2 (the Michaelis-Menton constant K_M (21)). Oxygen levels during Koegas deposition were likely around 10^{-13} atm (22) (the predicted O_2 levels for the atmosphere before the rise of cyanobacteria (23), dissolved O_2 would be $1.26*10^{-7}$ nM), but constrained by multiple sulfur isotope data to be at most lower than $10^{-5.7}$ atm (dissolved O_2 would be 2.6 nM) (22). We used these two estimates of atmospheric oxygen to determine the amount of manganese that could be oxidized at these low O_2 levels. Using the lowest reported value for measured biological Michaelis-Menton constants (K_M = 0.87μM (21)), the highest values for maximum Mn(II)-oxidation rates at infinite O_2 (V_{Max} = 50nM per hr (21)), we estimated a maximum rate of Mn oxide production using saturation kinetics calculations (21):

$$\text{Oxidation rate of Mn(II)} = (s * V_{Max}) / (K_M + s)$$

At the likely pre-cyanobacteria levels of 10^{-13} atm of O_2, the Mn oxidation rate is $7.24 * 10^{-9}$ nM per hr, or $3.48 * 10^{-9}$ g per L per kyr. At the highest permitted O_2 concentrations of $10^{-5.7}$ atm, the Mn oxidation rate is 0.151 nM per hr, or 0.073 g per L per kyr.

These rates can be considered in the context of the processes delivering sediment to this basin. Koegas Subgroup lithologies describe a mixed clastic-chemical sedimentary basin

with intercalated sequences of wave-modified deltaic siliciclastic sediments and iron formation (4, 5, 24). Iron formations here are often cross-bedded and granular, implying high wave action, and contain admixtures of sand, silt, and detrital aluminosilicate minerals, further indicating competing terrigenous detrital influxes and chemical sedimentation (5) (Fig. 3*A* and *B*). We estimate a seawater depth of approximately 10m for the GTF01 core, where sandstone intervals better constrain the water depth. Sedimentation rates can be approximated using measured rates for similar sedimentary basins and processes, with the assumption of uniform physical processes of sediment transport. Sadler (1981) constructed a vast compilation of ~25,000 rate measurements and determined that sedimentation rates vary depending on integration time span (25). With delta lobe switching occurring at approximately 3 to 1500 year intervals (26), terrigenous shelf delta and shelf seas sedimentation rates vary from ~300m per kyr to ~2m per kyr (27). We conservatively use 1m per kyr as the lowest background sediment accumulation rate during Mn deposition. Alternatively, Barley et al. (1997) estimated sedimentation rates for the deposition of banded iron formations in the Hamersley basin, a shallow marine platform of slightly older age in Western Australia, suggesting rates between 0.1 and 1 m per kyr using U-Pb zircon dating (interpolated from rates in m per myr). These rates have been used in other geobiological calculations for iron formation deposition (see (28)), and though it is an imperfect process and geodynamic basinal analog for the deposits examined here (as the Hamersley basin was a siliciclastic-starved marine platform without significant river detrital flux (29)), we also use these rates for comparison.

We converted our Mn oxidation rate calculations for different oxygen concentration scenarios into the mass of Mn deposited per thousand years and divided by the sediments accumulated in that time. A 10m-water column overlying a 1cm x 1cm square of sea floor is equal to 1 L of water in which Mn could be oxidized by O_2. For the same area, continental shelf sedimentation rates would predict 100cm^3 deposited in 1000 years (25), while the starved marine platform rates would estimate 10 to 100cm^3 per kyr (30). Mass of the sedimentary column can be determined using an average density of iron formations, 3.45 g cm^{-3}, from (31). Applying these calculations to the Mn rates determined above, at 10^{-13} atm, the percent Mn in the sediments is insignificant: the Mn oxides produced by O_2 are 1.01 * 10^{-9} % of the sediments using shelf seas and delta sedimentation rates and 1.01 * 10^{-8} % of the sediments using the lowest starved marine platform sedimentation rates. At the highest O_2 levels allowed by our proxies, Mn oxides are 0.02% of the sediments using the higher shelf rates and 0.2% of the sediments using the lower starved platform rates. Thus the nM dissolved oxygen concentrations maximally allowed by multiple sulfur isotopes are not sufficient for producing the Mn enrichments observed throughout our cores in both shallow and deep-water paleoenvironments. These calculations do not account for any Mn loss back to the water column from pore fluids during reduction. Including a fraction of recycled Mn in these kinetic calculations would just further highlight the discordance between the required rates and the exceedingly low O_2 concentrations indicated by the detrital pyrite and

anomalous sulfur isotope fractionations. Simply put, Mn oxidation by O_2—either abiologically or biologically—is too slow to account for our observed enrichments.

There are few other mechanisms to potentially oxidize manganese. Biological Mn oxidation using nitrate is thermodynamically feasible but does not appear to occur in nature (21, 32). Hydrogen peroxide can oxidize manganese, but production of a large volume of H_2O_2 would require a local source ice (33) and these deposits accumulated in a tropical paleolatitude (34). Photo-oxidation of manganese occurs at insignificant levels when dissolved iron is present (35). This points to photobiology as the process of Mn oxidation and concentration in the sediments.

SUPPORTING FIGURES

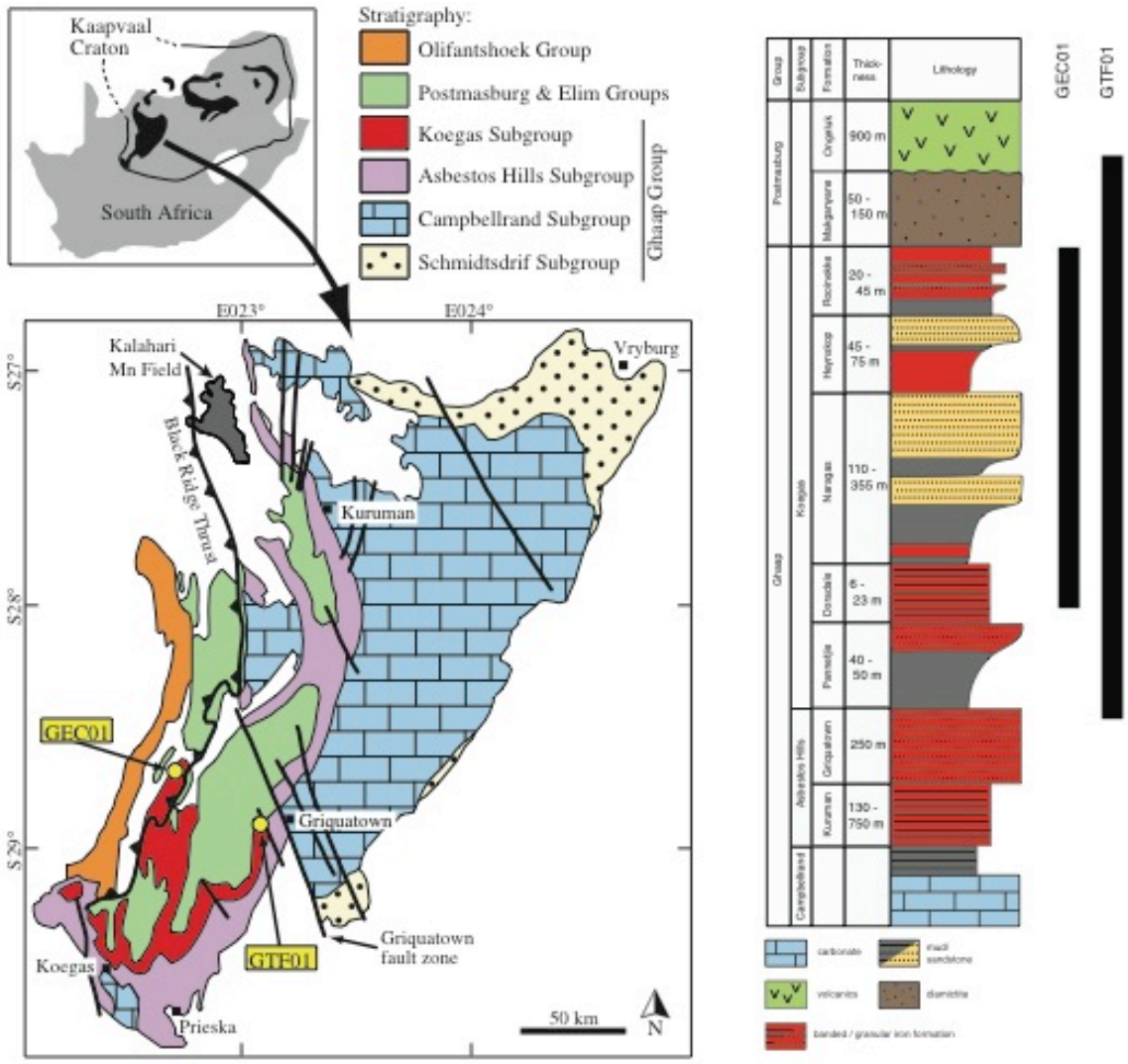

Figure S1: Geologic map of Archean and Paleoproterozoic-age strata exposed in Griqualand West sub basin of the Transvaal Supergroup, South Africa, modified from Schroder et al. (2011). Note the location of drill cores GTF01 and GEC01. To the right is a generalized stratigraphic column with lithologic information showing the stratigraphic breadth of the two drill cores.

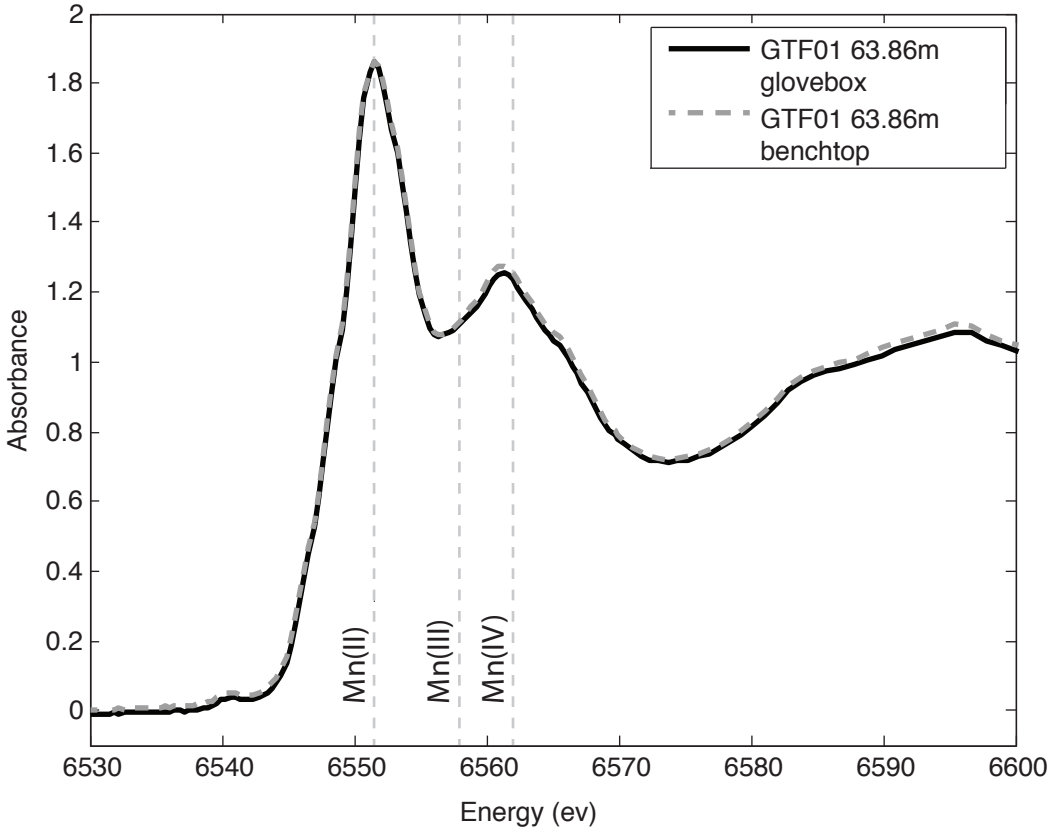

Figure S2: Bulk X-ray absorption spectra of one sample (GTF01 at 63.86m) prepared both in an anaerobic glovebox and on an aerobic benchtop and measured on beamline 4-3 at SSRL. Maximal absorptions for Mn(II), Mn(III), and Mn(IV) are shown for reference. Spectra are indistinguishable, indicating lack of Mn oxidation from exposure to oxygen over a timescale of ~ 1 week.

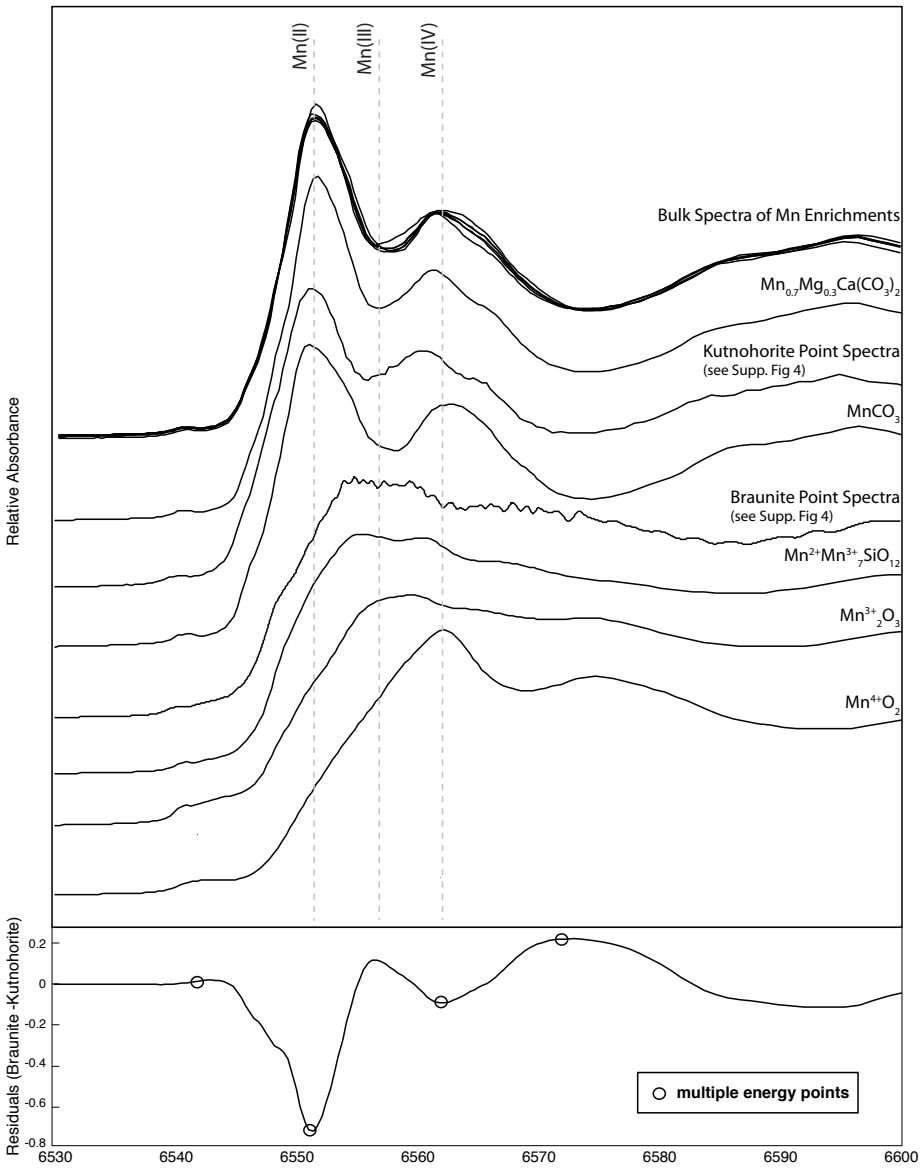

Figure S3: X-ray absorption spectra of known Mn-bearing minerals: well-characterized kutnohorite and braunite from the Kalahari Mn Field, rhodochrosite, and Mn(III) and Mn(IV) oxides. Mn(II) in carbonate phases show XANES spectra easily distinguishable from mixed valence manganese (II and III) in braunite [$Mn(II)Mn(III)_4(SiO_4)O_8$] and other species with oxidized Mn. Compare these to bulk spectra of all Koegas Mn enrichments from GEC01 and GTF01 (n=16) and point spectra from carbonate concretions and oxide matrix of the Kalahari. Bulk Koegas spectra and carbonate concretions from the Kalahari best match kutnohorite spectra. Also shown by vertical lines are maximal absorption energies of Mn(II), Mn(III), and Mn(IV). Lower panel plots residuals

when subtracting Kalahari kutnohorite from braunite. Black circles indicate the X-ray energies commonly used to distinguish Mn redox states.

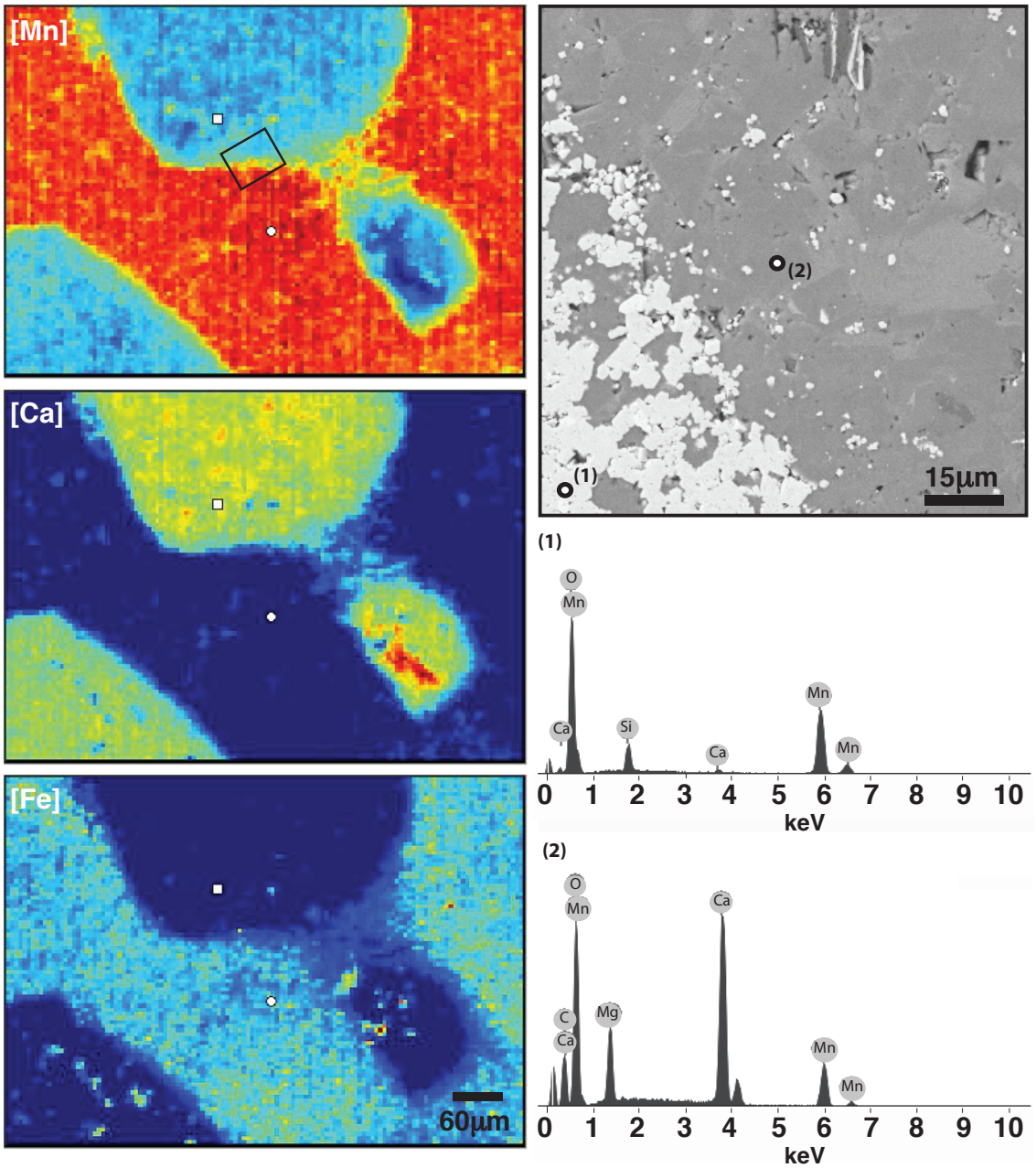

Figure S4: Left, X-ray fluorescence (XRF) maps of Mn, Ca, and Fe abundance on a sample from the Kalahari Manganese Field. Small white squares mark positions of spots where kutnohorite and braunite spectra were measured to obtain endmember spectra (Figure S3*A*) for multiple energy redox maps presented in Fig. 2. On the right, a SEM backscatter image of the domain highlighted in the black box on the left. EDS spectra on the first and second marked circles highlight the composition of braunite and kutnohorite, respectively.

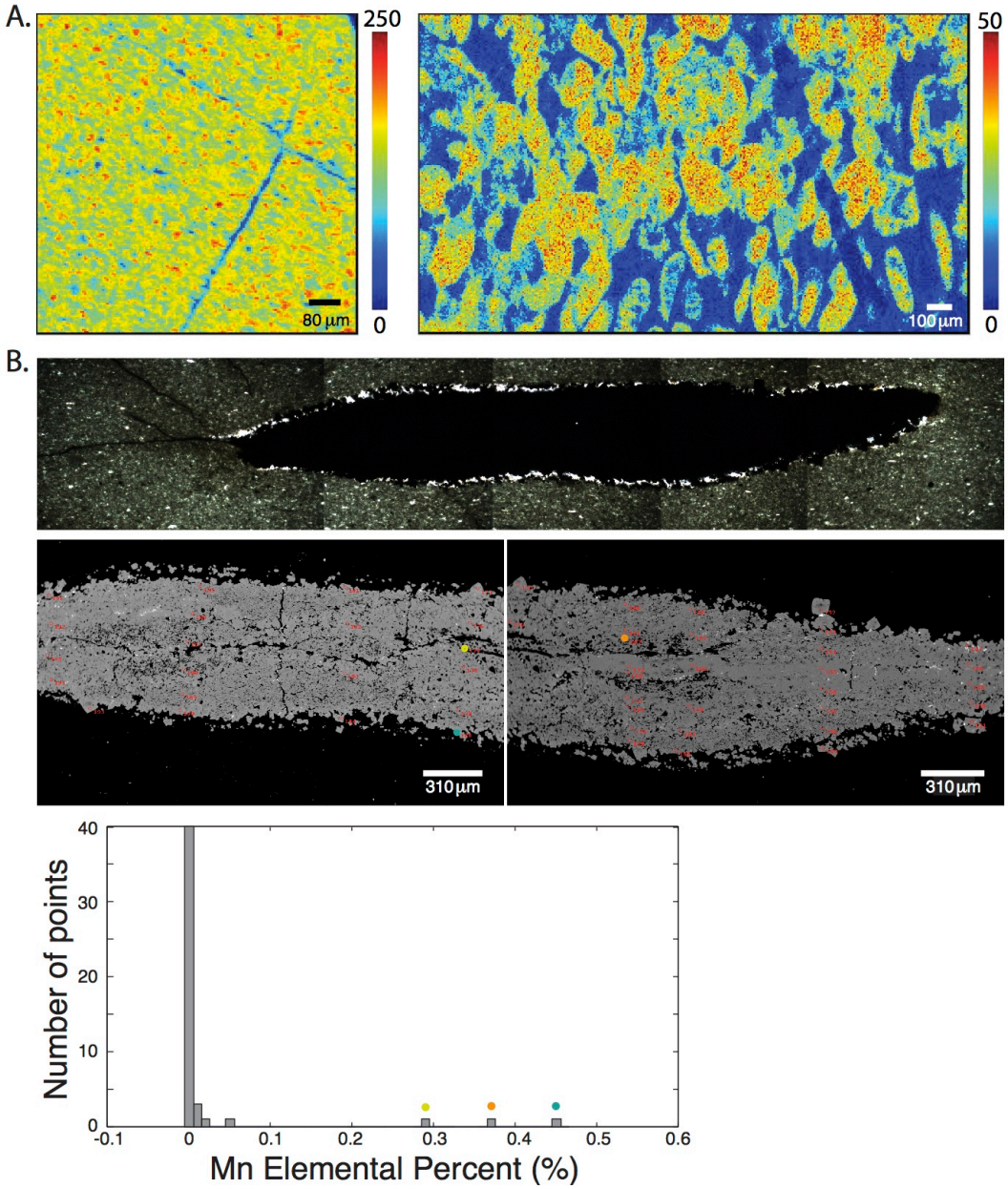

Figure S5: (A) Manganese concentration in µg/cm² measured by X-ray fluorescence at SSRL. Mn concentrations are much lower in mineralized late cracks and fractures, indicating that Mn enrichments did not originate from late fluids. (B) Transmitted light photomicrograph (above) and backscatter SEM image (below) of GEC01 169.83m showing discontinuous pyrite mineralization along a fracture. Bottom is a histogram of Mn concentration from electron probe measurements. Outliers with higher Mn abundance are shown as yellow, orange and blue dots. Note that the positions of these anomalous spot analyses occur in regions that incorporate more matrix and are not solely pyrite.

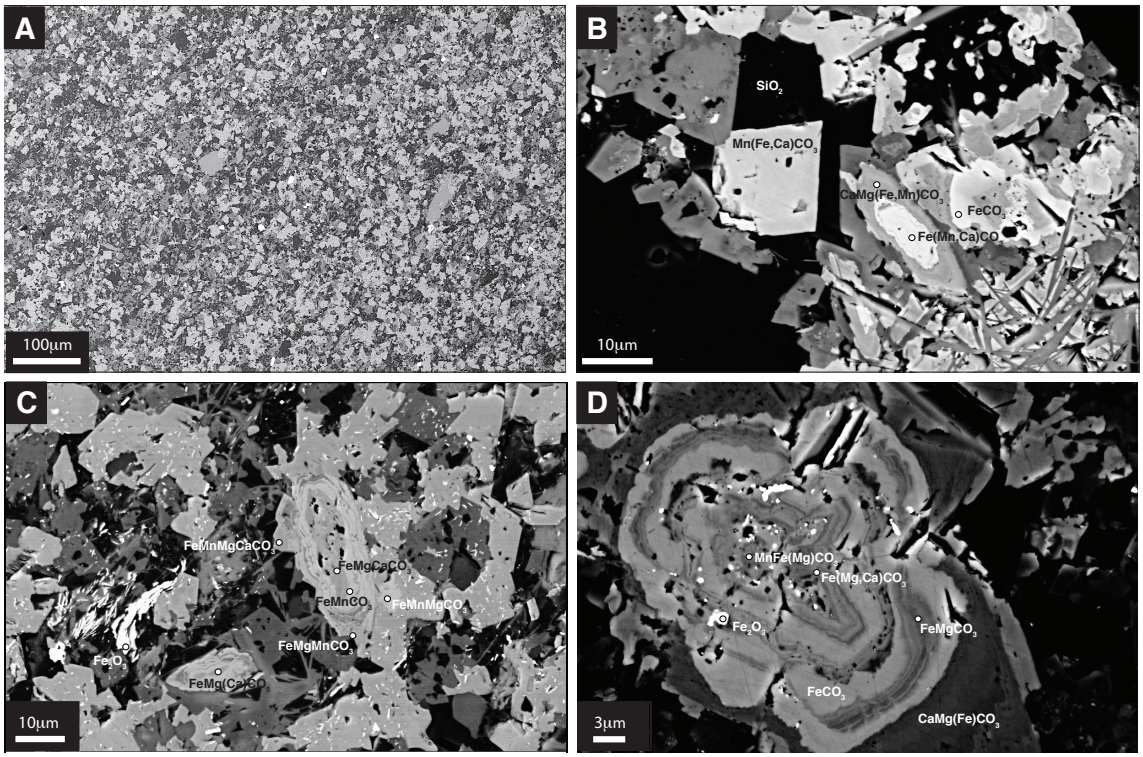

Figure S6: SEM backscatter images of samples enriched in Mn reveal very fine-grained mixtures of oxide, silicate, and carbonate phases with diagenetic textures. (A) and (C) from GTF 111.15m; (B) and (D) from GTF 54.10m.

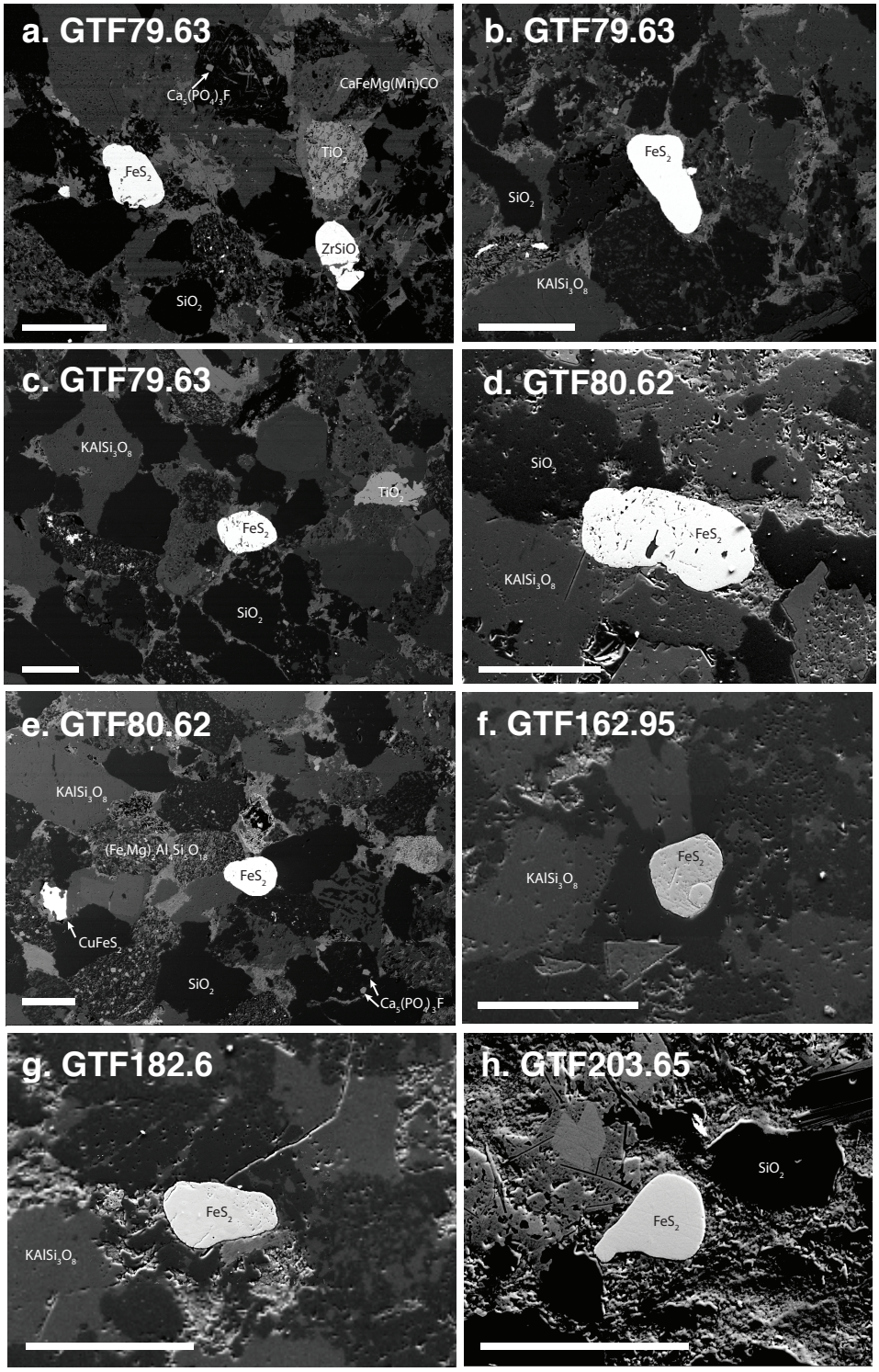

Figure S7: SEM backscatter images of detrital pyrite grains from sandstone subunits in GTF01. Note size, correlation with other heavy minerals, and rounding. Scale bars are 100μm.

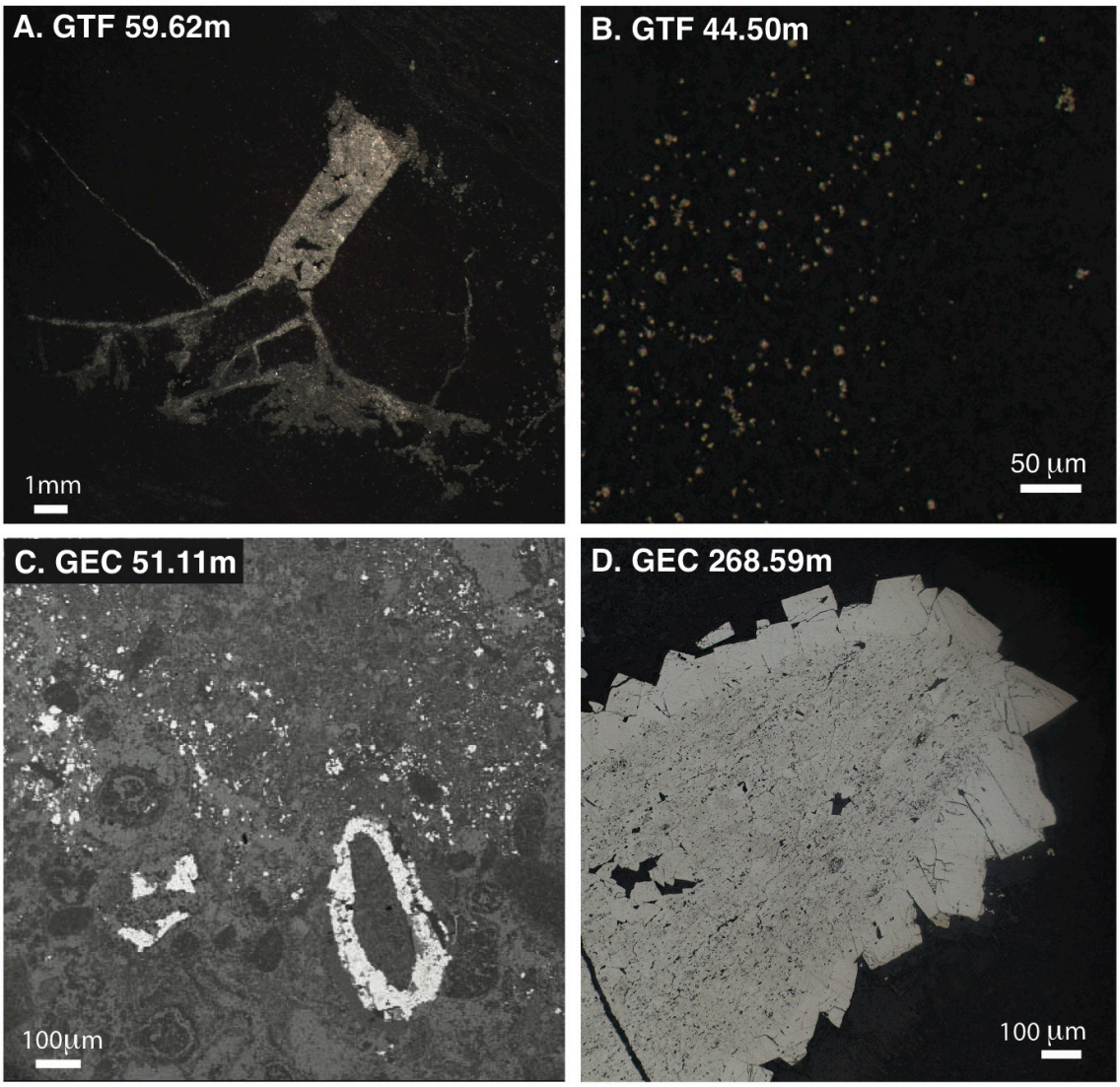

Figure S8: Photomicrographs from light and scanning electron microscopy highlighting examples of late pyrite textures. (A) GTF01 at 59.62m a fractured chert nodule hosting pyrite, (B) GTF01 at 44.50m shows finely disseminated but sharply euhedral grains, (C) GEC01 at 51.11m shows replacement of iron silicate and iron carbonate ooilitic grains by pyrite, (D) GEC01 at 268.59m shows a nodule with a coarse euhedral rim.

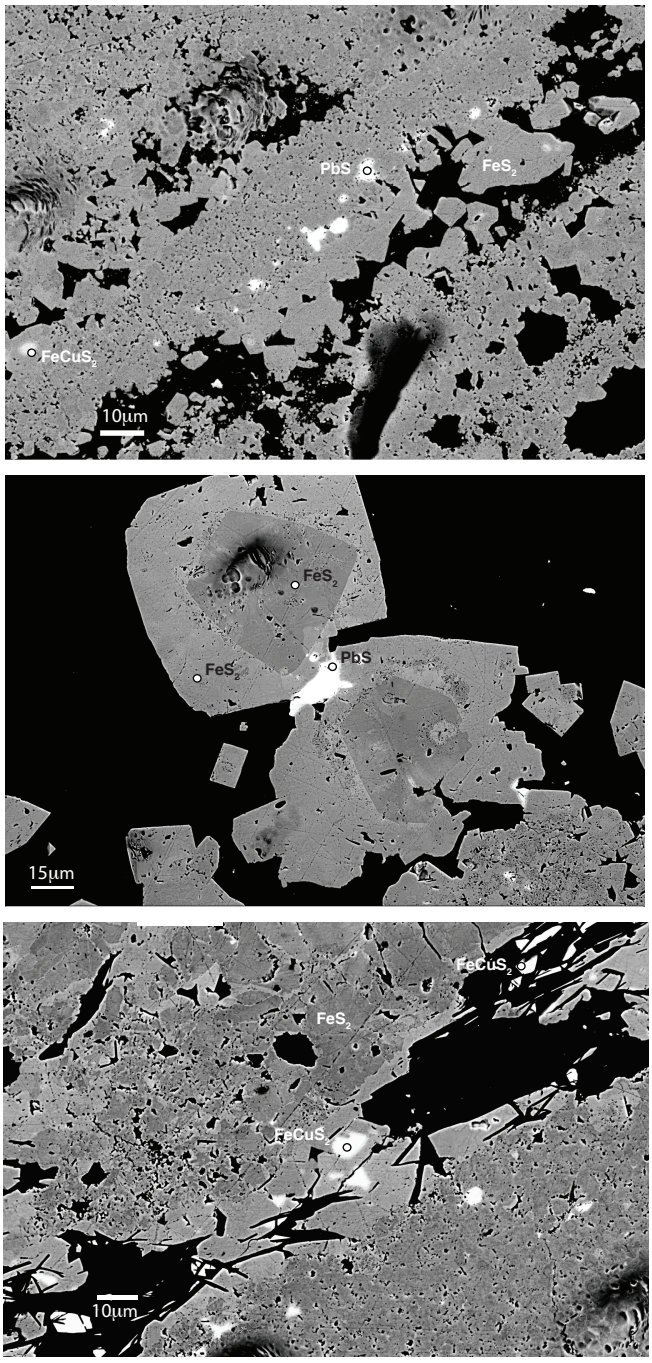

Figure S9: Backscatter electron photomicrographs of pyrites with late diagenetic textures and domains of chalcopyrite ($FeCuS_2$) and galena (PbS), highlighting several episodes of sulfide mineralization in these strata.

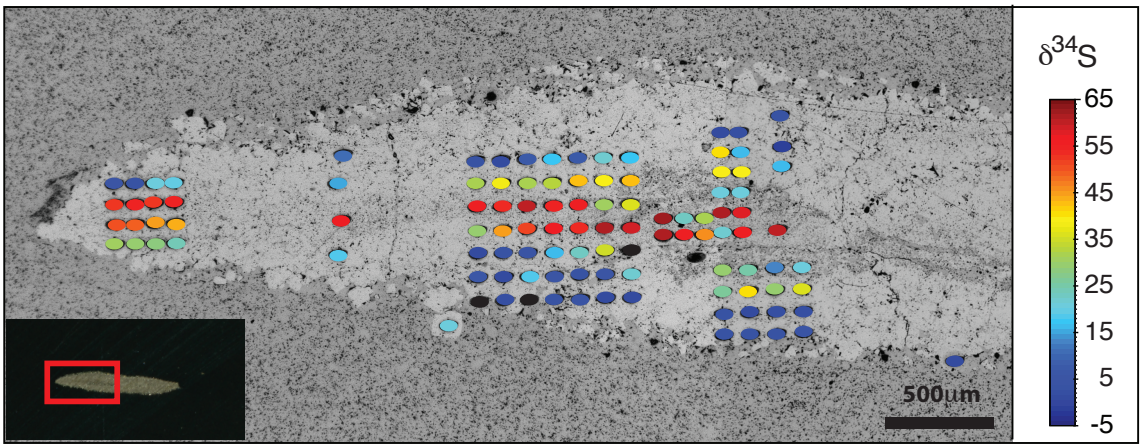

Figure S10: Example of *in situ* sulfur isotopic measurements from GEC01 at 169.83m on top of a backscatter electron image. This pyrite "nodule" is composed of aggregates of euhedral domains that grew from a through-going fracture. Color bar corresponds to $\delta^{34}S$ isotopic values (in permill VCDT), ranging from -5 to 65‰.

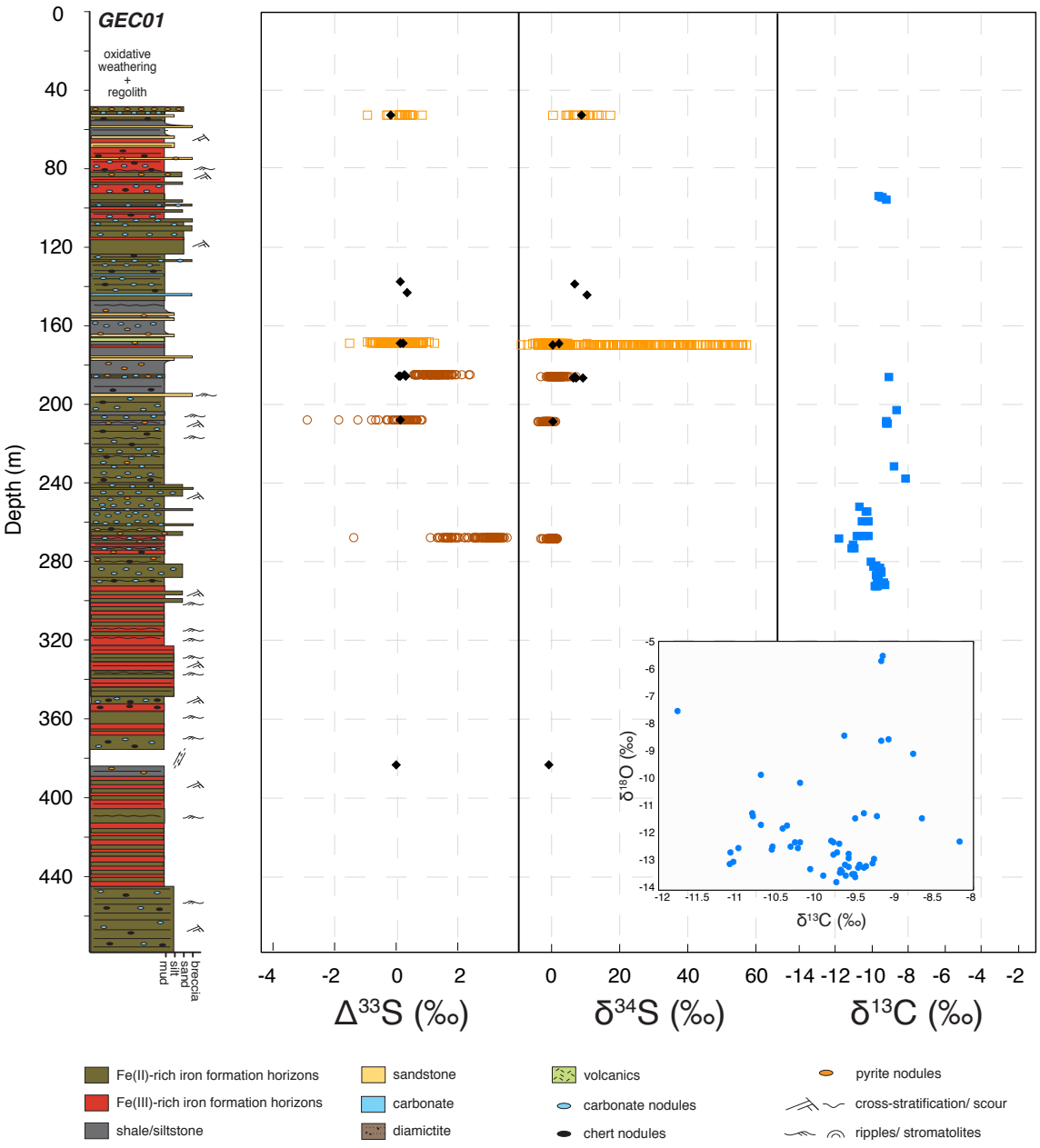

Figure S11: GEC01 core with sulfur isotopic data ($\Delta^{33}S$ and $\delta^{34}S$) and carbon isotopic data ($\delta^{13}C$; blue) plotted with depth. Maroon circles mark *in situ* primary pyrite, orange squares signify *in situ* measurements of late pyrite, and black diamonds designate bulk SF_6 measurements.

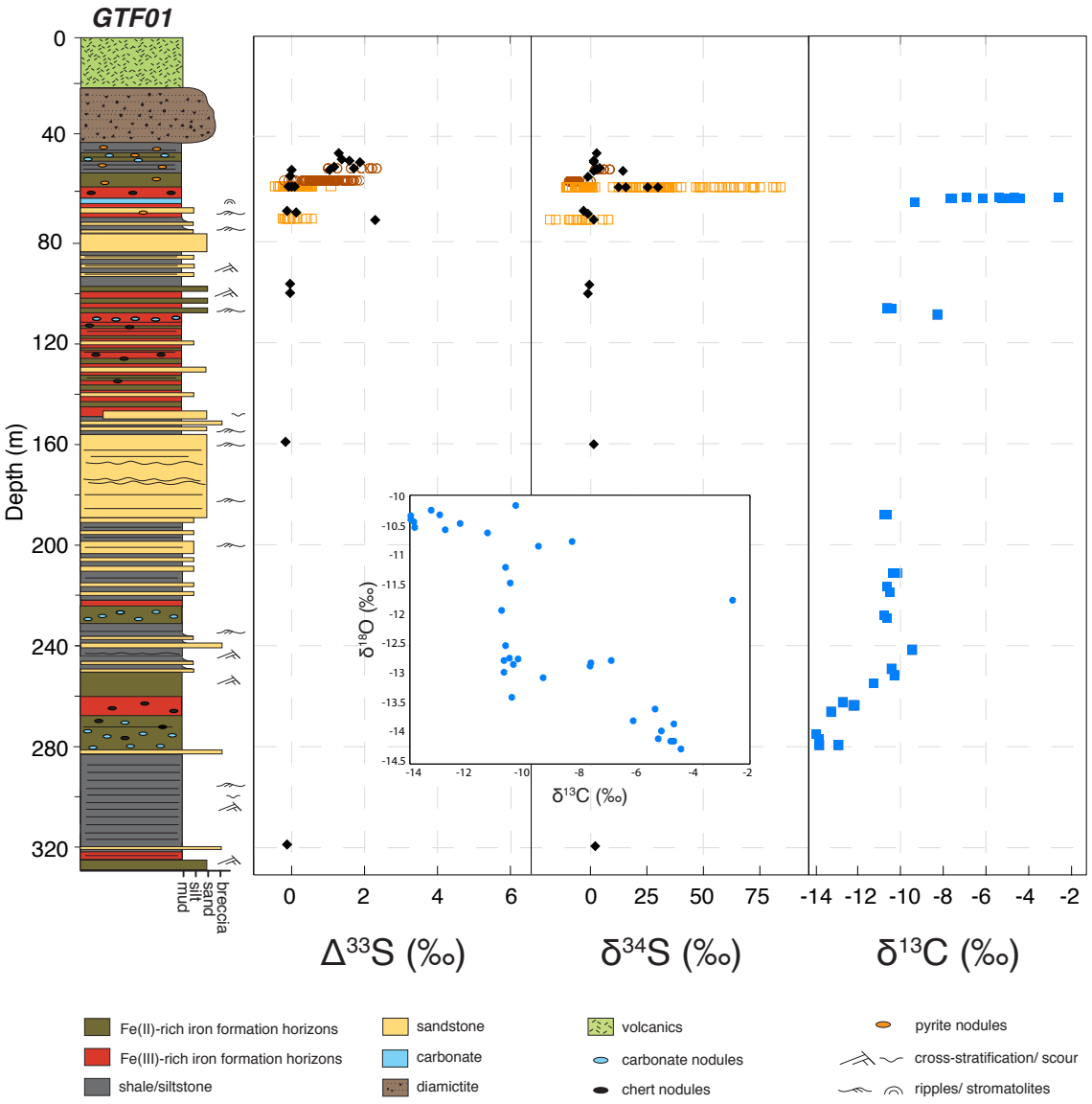

Figure S12: GTF01 core with sulfur isotopic data ($\Delta^{33}S$ and $\delta^{34}S$) and carbon isotopic data ($\delta^{13}C$; blue) plotted with depth. Maroon circles mark *in situ* primary pyrite, orange squares signify *in situ* measurements of late pyrite, and black diamonds designate bulk SF_6 measurements.

Table S1: Bulk Mn concentrations in weight percent at various depths from both cores (plotted in Fig. 1).

Core*	depth (m)	Mn (wt. %)		Core	depth (m)	Mn (wt. %)
GTF	42.65	0.2		GEC	41.15	0.4
GTF	45.53	1.9		GEC	53.2	0.82
GTF	47.65	16.6		GEC	64.3	0.31
GTF	54.1	10.1		GEC	65.9	0.51
GTF	55.9	0.5		GEC	69.15	0.04
GTF	57.35	0.6		GEC	74.09	0.147
GTF	58.45	0.3		GEC	82.2	0.52
GTF	60.73	0.6		GEC	82.8	0.37
GTF	63.8	1.8		GEC	84	0.32
GTF	64.12	2.1		GEC	87.5	0.66
GTF	64.45	0.6		GEC	89.6	1.8
GTF	68.2	0.7		GEC	90.4	3.57
GTF	74.18	0.2		GEC	92.96	4.14
GTF	80.62	0.3		GEC	93.5	9.04
GTF	90.12	4.4		GEC	93.6	7.92
GTF	100.15	0.4		GEC	94.5	12.3
GTF	108.4	7.8		GEC	97.71	0.915
GTF	110.7	7		GEC	99	0.583
GTF	111.15	4.9		GEC	103.38	0.246
GTF	111.75	1.5		GEC	118	0.45
GTF	114.68	0.5		GEC	120	1.01
GTF	128.47	0.1		GEC	122.5	0.17
GTF	136.16	0.1		GEC	126.5	0.28
GTF	141.8	0.3		GEC	128.5	0.05
GTF	148.3	0.3		GEC	135.5	0.15
GTF	151.22	0.1		GEC	140	0.18
GTF	151.22	1.3		GEC	144.3	0.18
GTF	160.4	0.3		GEC	152	0.07
GTF	163.1	0.1		GEC	159.83	0.16
GTF	169.54	0.2		GEC	164.5	0.39
GTF	178.45	0.2		GEC	166.5	0.04
GTF	183.92	0.1		GEC	172.5	0.3
GTF	193.06	0.1		GEC	181.1	0.45
GTF	210.08	0.2		GEC	188.4	0.49
GTF	218.76	0.3		GEC	202.5	3.04
GTF	220	1.4		GEC	209.4	3.16
GTF	221.75	2		GEC	216	4.76

GTF	223.5	2.5		GEC	231.7	3.94
GTF	224.7	3.6		GEC	233.3	2.16
GTF	225.1	1.3		GEC	247.9	0.645
GTF	225.2	0.5		GEC	249.82	0.54
GTF	228.9	5.8		GEC	253	6.3
GTF	229.25	6.2		GEC	257	1.01
GTF	229.6	7.1		GEC	259	3.2
GTF	229.8	10		GEC	259.87	0.569
GTF	229.92	10.4		GEC	267.4	7.95
GTF	230	11.6		GEC	271	4.16
GTF	230.05	5.5		GEC	279.6	0.04
GTF	233.7	0.5		GEC	280.19	0.179
GTF	238.7	1.1		GEC	282.45	0.173
GTF	243	3.7		GEC	284.7	0.94
GTF	251.06	1.5		GEC	296.22	0.596
GTF	251.06	0.4		GEC	296.27	0.758
GTF	251.88	0.9		GEC	300	0.64
GTF	253	2.2		GEC	308.84	0.879
GTF	254.8	1.3		GEC	318.18	4.52
GTF	257.65	0.7		GEC	339.59	0.24
GTF	260.08	0.7		GEC	363.1	0.59
GTF	265.62	1				
GTF	267	1				
GTF	274.24	1.4				
GTF	279.8	0.7				
GTF	281.4	0.2				
GTF	284.65	0.3				
GTF	285.5	0.5				
GTF	289.61	0.1				
GTF	298.65	0.1				
GTF	309.74	0.1				
GTF	316.8	0.1				
GTF	318.56	0.1				
GTF	324.6	0.7				
GTF	327.22	0.5				

*some GTF data from Ref (9).

Table S2: $\delta^{13}C$ and $\delta^{18}O$ data at various depths from both cores (plotted in Fig. 3*C* and Fig. S11 and S12).

Core	depth	$\delta^{13}C$	$\delta^{18}O$		Core	depth	$\delta^{13}C$	$\delta^{18}O$
GTF	63.95	-5.33	-13.59		GEC	92.98	-9.64	-8.42
GTF	63.96	-6.88	-12.78		GEC	93.5	-9.5	-11.41
GTF	63.97	-4.68	-13.84		GEC	93.6	-9.39	-11.24
GTF	64.02	-2.58	-11.85		GEC	94.49	-9.22	-11.34
GTF	64.02	-2.6	-11.68		GEC	185.58	-9.07	-8.56
GTF	64.14	-5.12	-14.02		GEC	202.5	-8.65	-11.41
GTF	64.14	-5.12	-13.89		GEC	208.48	-9.17	-8.6
GTF	64.15	-4.42	-14.26		GEC	209.4	-9.15	-5.55
GTF	64.2	-5.21	-14.09		GEC	209.4	-9.17	-5.73
GTF	64.22	-6.11	-13.79		GEC	231.7	-8.76	-9.08
GTF	64.25	-7.62	-12.87		GEC	238.13	-8.17	-12.25
GTF	64.3	-4.68	-14.12		GEC	252.52	-10.7	-11.64
GTF	64.35pink	-7.61	-12.81		GEC	253.01	-11.02	-11.71
GTF	64.35white	-4.78	-14.13		GEC	254.49	-10.32	-12.45
GTF	65.82pink	-9.29	-13.06		GEC	254.49	-10.26	-12.28
GTF	107.86	-10.67	-12.78		GEC	259.75	-10.23	-12.48
GTF	107.92	-10.4	-13.39		GEC	259.75	-10.2	-12.28
GTF	110.22	-8.25	-10.78		GEC	259.75	-10.56	-12.55
GTF	189.66	-10.74	-12.92		GEC	259.75	-10.55	-12.44
GTF	189.66	-10.63	-13.03		GEC	267.31	-10.42	-11.79
GTF	212.45	-10.35	-12.84		GEC	267.31	-10.36	-11.67
GTF	212.57	-10.18	-12.74		GEC	267.4	-10.8	-11.34
GTF	212.57	-10.16	-12.76		GEC	267.4	-10.81	-11.23
GTF	217.52	-10.61	-12.52		GEC	267.43	-10.2	-10.13

GTF	219.99	-10.48	-12.74		GEC	267.49	-10.7	-9.83
GTF	228.8	-10.75	-11.94		GEC	268.59	-11.76	-7.52
GTF	230.1	-10.62	-11.22		GEC	271.65	-11.05	-13
GTF	243	-9.45	-10.86		GEC	273.38	-10.98	-12.48
GTF	250.27	-10.45	-11.47		GEC	273.38	-11.08	-12.66
GTF	253	-10.26	-10.18		GEC	273.38	-11.09	-13.07
GTF	255.94	-11.25	-10.63		GEC	280.66	-10.07	-13.25
GTF	263.53	-12.73	-10.59		GEC	282.64	-9.74	-13.73
GTF	265.17	-12.24	-10.55		GEC	283.38	-9.9	-13.5
GTF	265.17	-12.18	-10.41		GEC	283.99	-9.62	-13.48
GTF	267.47	-13.25	-10.26		GEC	283.99	-9.53	-13.44
GTF	276.27	-13.95	-10.35		GEC	283.99	-9.51	-13.43
GTF	276.27	-13.95	-10.41		GEC	285.81	-9.58	-13.18
GTF	278	-13.84	-10.45		GEC	285.81	-9.46	-13.19
GTF	280.28	-12.94	-10.34		GEC	285.81	-9.44	-13.09
GTF	280.38	-13.81	-10.55		GEC	286.05	-9.5	-13.53
					GEC	286.55	-9.58	-12.86
					GEC	286.55	-9.58	-12.71
					GEC	287.71	-9.77	-12.73
					GEC	287.71	-9.73	-12.64
					GEC	291.04	-9.68	-13.28
					GEC	291.04	-9.63	-13.1
					GEC	291.04	-9.66	-13.35
					GEC	291.04	-9.69	-13.39
					GEC	291.09	-9.36	-13.16
					GEC	292.2	-9.39	-13.21
					GEC	292.2	-9.28	-13.03
					GEC	292.2	-9.26	-12.88
					GEC	292.88	-9.77	-12.29
					GEC	292.88	-9.8	-12.24
					GEC	292.88	-9.7	-12.34

SUPPORTING REFERENCES

1. Pickard A. (2003) SHRIMP U–Pb zircon ages for the Palaeoproterozoic Kuruman Iron Formation, Northern Cape Province, South Africa: evidence for simultaneous BIF deposition on Kaapvaal and Pilbara Cratons. *Precambrian Research* 125:275–315.

2. Trendall AF et al. (1990) in *Proceedings of the Third International Archaean Symposium* (Geological Society of Australia, Perth), pp 81–83.

3. Nelson DR, Trendall AF, Altermann W (1999) Chronological correlations between the Pilbara and Kaapvaal cratons. *Precambrian Research* 97:165–189.

4. Beukes NJ (1983) in *Developments in Precambrian Geology*, eds Trendall AF, Morris RC (Elsevier), pp 131–198. Available at: http://www.sciencedirect.com/science/article/pii/S0166263508700434 [Accessed March 22, 2013].

5. Schröder S, Bedorf D, Beukes NJ, Gutzmer J (2011) From BIF to red beds: Sedimentology and sequence stratigraphy of the Paleoproterozoic Koegas Subgroup (South Africa). *Sedimentary Geology* 236:25–44.

6. Kirschvink JL et al. (2000) Paleoproterozoic snowball Earth: Extreme climatic and geochemical global change and its biological consequences. *PNAS* 97:1400–1405.

7. Walraven F, Armstrong R., Kruger F. (1990) A chronostratigraphic framework for the north-central Kaapvaal craton, the Bushveld Complex and the Vredefort structure. *Tectonophysics* 171:23–48.

8. Armstrong RA (1987) Geochronological Studies on Archean and Proterozoic Formations of the Namaqua Front and Possible Correlates on the Kaapvaal Craton [Ph.D. Thesis].

9. Cornell DH, Schütte SS, Eglington BL (1996) The Ongeluk basaltic andesite formation in Griqualand West, South Africa: submarine alteration in a 2222 Ma proterozoic sea. *Precambrian Research* 79:101–123.

10. Gutzmer, Jens, Beukes, Nicolas (1998) *High-grade manganese ores in the Kalahari manganese field: characterisation and dating of ore forming events* (Rand Afrikaans University, Johannesburg).

11. Beukes NJ, Gutzmer J (2008) in *Banded Iron Formation-Related High-Grade Ore*, eds Hagemann S, Rosiere C, Gutzmer J, Beukes N, pp 5–47.

12. Polteau S, Moore JM, Tsikos H (2006) The geology and geochemistry of the Palaeoproterozoic Makganyene diamictite. *Precambrian Research* 148:257–274.

13. Hoffman PF (2013) The Great Oxidation Event and a Siderian Snowball Earth: MIF based correlation of Paleoproterozoic glaciations. *Chemical Geology* in press.

14. Morgan JJ (2005) Kinetics of reaction between O2 and Mn(II) species in aqueous solutions. *Geochimica et Cosmochimica Acta* 69:35–48.

15. Webb SM (2011) The MicroAnalysis Toolkit: X-ray Fluorescence Image Processing Software. *AIP Conference Proceedings* 1365:196–199.

16. Mayhew LE, Webb SM, Templeton AS (2011) Microscale imaging and identification of Fe speciation and distribution during fluid-mineral reactions under highly reducing conditions. *Environ Sci Technol* 45:4468–4474.

17. Bekker A et al. (2001) Chemostratigraphy of the Paleoproterozoic Duitschland Formation, South Africa: Implications for Coupled Climate Change and Carbon Cycling. *Am J Sci* 301:261–285.

18. Fischer WW et al. (2009) Isotopic constraints on the Late Archean carbon cycle from the Transvaal Supergroup along the western margin of the Kaapvaal Craton, South Africa. *Precambrian Research* 169:15–27.

19. Luther GWI (2010) The Role of One- and Two-Electron Transfer Reactions in Forming Thermodynamically Unstable Intermediates as Barriers in Multi-Electron Redox Reactions. *Aquatic Geochemistry* 16:395–420.

20. Broecker WS, Peng T-H (1982) *Tracers in the Sea* (Eldigio Pr, Columbia University, Palisades, New York).

21. Clement BG, Luther III GW, Tebo BM (2009) Rapid, oxygen-dependent microbial Mn(II) oxidation kinetics at sub-micromolar oxygen concentrations in the Black Sea suboxic zone. *Geochimica et Cosmochimica Acta* 73:1878–1889.

22. Pavlov AA, Kasting JF (2002) Mass-Independent Fractionation of Sulfur Isotopes in Archean Sediments: Strong Evidence for an Anoxic Archean Atmosphere. *Astrobiology* 2:27–41.

23. Kasting JF (1993) Earth's early atmosphere. *Science* 259:920–926.

24. Beukes NJ (1978) Die karbonaatgesteentes en ysterformasies van die Ghaap-Groep van die Transvaal-Supergroep in Noord-Kaapland.

25. Sadler P (1981) Sediment Accumulation Rates and the Completeness of Stratigraphic Sections. *Journal of Geology* 89:569–584.

26. Jerolmack DJ, Mohrig D (2007) Conditions for branching in depositional rivers. *Geology* 35:463–466.

27. Sadler PM, Hass HC (1999) in *On the determination of sediment accumulation rates*, ed Bruns P (Trans Tech Publications, Switzerland), pp 15–40.

28. Konhauser KO et al. (2002) Could bacteria have formed the Precambrian banded iron formations? *Geology* 30:1079–1082.

29. Blake TS, Barley ME (1992) Tectonic evolution of the Late Archaean to Early Proterozoic Mount Bruce Megasequence Set, western Australia. *Tectonics* 11:1415–1425.

30. Barley ME, Pickard AL, Sylvester PJ (1997) Emplacement of a large igneous province as a possible cause of banded iron formation 2.45 billion years ago. *Nature* 385:55–58.

31. Ewers WE, Morris RC (1981) Studies of the Dales Gorge Member of the Brockman Iron Formation, Western Australia. *Economic Geology* 76:1929–1953.

32. Schippers A, Neretin LN, Lavik G, Leipe T, Pollehne F (2005) Manganese(II) oxidation driven by lateral oxygen intrusions in the western Black Sea. *Geochimica et Cosmochimica Acta* 69:2241–2252.

33. Liang M-C, Hartman H, Kopp RE, Kirschvink JL, Yung YL (2006) Production of hydrogen peroxide in the atmosphere of a Snowball Earth and the origin of oxygenic photosynthesis. *Proc Natl Acad Sci USA* 103:18896–18899.

34. Evans DA, Beukes NJ, Kirschvink JL (1997) Low-latitude glaciation in the Palaeoproterozoic era*, Published online: 20 March 1997; | doi:101038/386262a0* 386:262–266.

35. Anbar AD, Holland HD (1992) The photochemistry of manganese and the origin of banded iron formations. *Geochimica et Cosmochimica Acta* 56:2595–2603.